Materials & Design 254 (2025) 114105

Contents lists available at ScienceDirect

Materials & Design

journal homepage: www.elsevier.com/locate/matdes

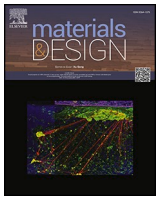

Hybrid piezo-, pyro-, and triboelectric nanogenerator based on PVDF and rGO composite fibers for a multifunctional approach to energy harvesting applications

Sunija Sukumaran [a], Piotr K. Szewczyk [a], Tomasz Bajda [b], Urszula Stachewicz [a,*]

[a] Faculty of Metals Engineering and Industrial Computer Science, AGH University of Krakow 30-059 Krakow, Poland
[b] Faculty of Geology, Geophysics and Environmental Protection, AGH University of Krakow 30-059 Krakow, Poland

ARTICLE INFO

Keywords:
PVDF
Reduced graphene oxide
Piezoelectricity
Triboelectricity
Pyroelectricity
Energy harvesting

ABSTRACT

Recently, wearable nanogenerators have gained interest in energy harvesting and sensors, driven by smart electronics and Internet of Things (IoT) advancements. Here, we have developed a multifunctional nanogenerator that can convert mechanical and thermal energy into electrical energy via piezoelectric, triboelectric, and pyroelectric effects. The electrospun nanogenerator was fabricated to investigate the effect of reduced graphene oxide (rGO) on the energy generation of polyvinylidene fluoride (PVDF) fibers. The highest amount of electroactive β phase (81 %) and crystallinity (48.58 %) were obtained for 7 wt% rGO/PVDF fiber composite. Then, the 7 wt% rGO/PVDF composite was taken to prepare the piezo, tribo, and pyroelectric nanogenerator, and characterized using piezoresponse force microscopy (PFM), Kelvin probe microscopy (KPFM), and scanning thermal microscopy (SThM). Furthermore, the nanogenerator was made using the composite mat, illustrating its potential for powering small electronic devices using piezoelectric power and an enormous triboelectric power density of 3.37 ± 0.72 $mWcm^{-2}$. We also demonstrate the device's multifunctionality under thermal fluctuations. The results show the synergetic tribo and pyroelectric current of 33nA from 7 wt% rGO/PVDF. The present work indicates the significance of rGO inclusion into a PVDF matrix, resulting in enhanced multifunctional properties for energy harvesting, thereby enabling self-powering capabilities for microelectronic devices.

1. Introduction

The increasing demand for sustainable energy has led to academic and industrial endeavors in various fields, such as smart textiles, healthcare, robotics, the Internet of Things (IoT), wireless technologies, and portable/wearable electronics [1–3]. Attaining a sustainable power source to supply power to smart electronic devices is attractive due to its potential to mitigate the additional costs and time associated with managing chemical batteries [4,5]. In this context, energy harvesting technologies that can scavenge energy from the surrounding environment are appealing areas for realizing self-powered microelectronic devices [6,7].

Among the several energy harvesting techniques, mechanical energy scavenging, which converts wasted mechanical energy, such as vibrations from machines and human motions, into useful electrical energy, has gained widespread applications [8,9]. For mechanical energy conversion, piezoelectric and triboelectric effects stand out among the other energy harvesting techniques [10,11]. They have garnered substantial interest owing to their prospective applications in designing flexible, wearable, autonomous devices [10,12]. Piezoelectric materials produce an electric charge under the application of mechanical stress. Piezoelectric nanogenerators (PENG) found immense research attention in mechanical energy harvesting due to their high flexibility, easy processing, and use in organic optoelectronics, flexible electronics, and sensors [5,6,13]. However, the output performance of the PENG is not enough to power micro-electronic devices autonomously [9,12]. Triboelectric nanogenerators (TENG) work based on the triboelectric effect, which has a higher power output generation and a high energy conversion efficiency (85 %) [12,14]. They operate due to contact electrification and electrostatic induction, which occur between two materials possessing varying electron affinities, facilitating the conversion of mechanical energy into electrical energy [15,16]. TENG's lightweight, cost-effectiveness, flexibility, and ease of integration into many devices make it a promising candidate for scavenging energy

* Corresponding author.
E-mail address: ustachew@agh.edu.pl (U. Stachewicz).

https://doi.org/10.1016/j.matdes.2025.114105
Received 21 January 2025; Received in revised form 16 April 2025; Accepted 14 May 2025
Available online 14 May 2025

under various small mechanical and biomechanical actions [3,17,18].

Apart from mechanical energy, heat is another vastly available energy source in our ambient environment. Converting thermal energy into electrical energy also found significant research interest in low-power devices [19,20]. This energy conversion is commonly achieved using thermoelectric or pyroelectric effects [21]. Thermoelectric generators work based on the Seebeck effect; a temperature gradient is needed, and a small percentage of the heat is converted to electricity. Nonetheless, this kind of generator cannot function in an environment with temperature variations in time [22,23]. On the other hand, pyroelectric nanogenerators (PyNG) can convert temperature fluctuations into electric energy [22,23]. Numerous materials possess piezoelectric, triboelectric, and pyroelectric properties; this opens an opportunity to create a multifunctional material that, in turn, harvests mechanical and thermal energy simultaneously or even discreetly [22,24,25]. Also, it increases the possibilities of transforming various available energy sources available in the surrounding environment. In this regard, a ferroelectric fluoropolymer such as PVDF is an ideal choice for fabricating nanogenerators due to its excellent mechanical flexibility, lightness, and reversible piezo and pyroelectric properties [26,27].

Poly (vinylidene fluoride) (PVDF) is a multifunctional fluoropolymer that depicts superior piezoelectric and pyroelectric properties among other polymers, as well as acts as a triboelectric material [26,28]. However, it is essential to enhance the piezo and pyroelectric performance of PVDF by the formation of an electroactive β phase, which is responsible for the piezoelectric behavior, where the dipoles are oriented in all trans (TTTT) planar zig-zag confirmation [29,30]. Several strategies are employed to attain and improve the β phase of PVDF, such as polarization at a high electric field, mechanical stretching, annealing, and incorporation of fillers [31–33]. Electrospinning is a versatile technique to induce the formation of the β phase in PVDF through a single-step combined electrical poling and mechanical stretching under a high potential, leading to the nucleation of the β phase [31,34]. To date, many research works have been carried out to increase the piezoelectric properties of PVDF by including different fillers [32]. In the case of developing a multifunctional nanogenerator, the choice of the filler plays a vital role, as it should improve both electrical and thermal properties. Accordingly, carbon-based materials such as graphene oxide (GO) and reduced graphene oxide (rGO) conductive fillers are the ideal candidates due to their high electrical and thermal conductivity, surface area, and mechanical properties [35,36]. Besides the β phase enhancement, conductive fillers aid in increasing the transfer of induced charge, which directly influences the generated electrical power performance [37,38]. Compared to GO, rGO has higher thermal and electrical conductivity due to the fewer functional groups attached to the carbon atoms [37,39]. Thus, a composite from rGO and PVDF can be utilized to harvest different forms of energy. Zi et al. [40]., fabricated a hybrid PVDF based sensor able to harvest piezo, tribo and pyroelectric power. However, it lacks information regarding microscopic analysis, and the combined piezo and tribo properties were studied [41–43]. This is the first time we have presented the PVDF fiber with conductive filler like rGO's effects on the piezo, tribo, and pyroelectric properties for energy generation. Hybrid piezo/tribo energy harvesting devices were reported in the literature. However, a proper distinction between the piezo, tribo, and pyroelectric energy generation performance in electrospun fiber has not been reported yet. Therefore, in this study, we compare these three effects on electrospun PVDF/rGO composite to verify which one effectively enhances the energy harvesting performance of PVDF fiber.

This study incorporates different weight percentages of rGO filler (1, 5, 7, 10 wt%) into electrospun PVDF fibers and studies their structural and morphological properties. To the best of our knowledge, a higher amount of rGO fillers have been added to PVDF fiber for the first time in the literature. 7 wt% rGO filler inclusion remarkably increases the amount of an electroactive β phase in PVDF, which is useful for effective mechanical and thermal energy harvesting performance. We are not focusing on a new synthesis or fabricating method through this work. Rather, we focused on the mechanism behind the three major piezo-, tribo-, and pyroelectric energy harvesting techniques on micro and macroscopic scales. Also, we distinguish the piezo and triboelectric effects when subjected to mechanical stress. For the first time, we investigated the thermal conductivity of a single fiber and its correlation with the pyroelectric behavior of the composite mat. For the first time in literature, we are presenting a comprehensive study on micro and macroscopic level piezo, tribo, and pyroelectric characterization of the single fibers and fiber mats of PVDF and PVDF/rGO composites fiber to show the best energy harvesting performance in terms of power generation from PENG, TENG, and PyNG. Here, we have studied, constructed, and tested the nanogenerator capable of harvesting energy from various environments.

2. Materials and methods

2.1. Solution preparation and electrospinning

PVDF pellets (Mw = 275,000 $gmol^{-1}$, Sigma-Aldrich, UK) were dissolved in dimethylacetamide (DMAc, analytical standard, Avantor, Poland) and acetone (analytical standard, Avantor, Poland) in a 1:1 ratio to prepare a polymer solution with 24 wt% concentration [29,31]. The solution was constantly stirred at 650 rpm for 4 h on a hot plate (IKA RCT basic, Germany) at a temperature set to 55 ℃. The PVDF/rGO solutions containing different rGO (thickness 0.5–2 nm, Nanografi, Turkey) weight percentages (1 %, 5 %, 7 %,10 % wt%) were prepared as follows. First, the calculated amount of rGO was dispersed in DMAc and acetone (1:1) ratio by ultrasonication for 4 h (Emag, Emmi-E20, Germany) to avoid the agglomeration of rGO particles. Afterward, the dispersed rGO solution was mixed with the PVDF solution at 55 ℃ with constant stirring for 2 h. Finally, the PVDF/rGO solutions were ultrasonicated for 2 h prior to electrospinning.

The electrospinning of PVDF and the PVDF-rGO composites solutions was performed using an SKE electrospinner (Italy) with a climate control system. The PVDF fibers were produced by subjecting a positive voltage polarity of + 20 kV to the stainless needle (outer diameter of 0.8 mm and inner diameter of 0.5 mm). The distance between the stainless needle and the grounded collector was kept at 18 cm with a feeding rate of 1 mlh^{-1}. During electrospinning, the temperature and relative humidity (RH) were kept constant at 25 °C and 30 % for PVDF and PVDF/rGO composites. The electrospinning parameters for PVDF/rGO composites with different rGO wt% are listed in Table S1 of the Supplementary information (SI). The electrospun fiber mats were deposited on Al foil for SEM, FTIR, DSC, and XRD studies. For single fiber characterization techniques such as PFM, KPFM, and SThM analysis, the fibers were electropsun on ITO substrate (Ossila, Germany). All the AFM measurements were carried out by fixing the samples on a metallic stage and ensuring a conductive path using a silver paste. The same samples were used for all the AFM experiments to maintain the uniformity of the sample.

2.2. Characterization and measurements

Scanning Electron Microscopy (SEM): Using SEM (Merlin Gemini II, Zeiss, Germany), the fibers' morphology was imaged with an accelerating voltage of 3 kV at a working distance of 5.8 mm. Before imaging, all samples were coated with Au with a thickness of 8 nm using a rotary pump sputter coater (Q150RS, Quorum Technologies, UK). The ImageJ (v. 1.53c, USA) software was utilized to measure the fiber diameter (D_f) from the SEM micrographs.

Fourier Transform Infrared Spectroscopy (FTIR): FTIR was carried out to distinguish the various phases in PVDF and analyze the β phase content. The Nicolet iS5 FT-IR spectrophotometer (Thermo Fisher Scientific, Waltham, MA, USA), with a germanium crystal, was used to conduct the spectroscopy using the ATR technique. Over the

wavenumber range from 600 to 1800 cm^{-1}, 64 spectra were repeated with a resolution of 1 cm^{-1} for measurements.

A Differential Scanning Calorimeter (DSC): DSC (Mettler Toledo, Columbus, OH, USA) was used to perform the thermal characterization of the samples at a temperature range of 50 to 250 ℃ with a heating rate of 10 $K{\cdot}min^{-1}$. The measurements were carried out in a dynamic Ar atmosphere by placing the samples in an Al pan.

X-ray diffraction (XRD): The phase composition of the samples was determined by powder XRD using a SmartLab RIGAKU diffractometer (RIGAKU, Tokyo, Japan). The analysis was performed with graphite-monochromatized CuKα radiation operating at 9 kV. The measurements were conducted at 10–50° 2Θ with a measuring step of 0.05° $2\Theta s^{-1}$.

Conductometer: A Mettler Toledo conductometer (SevenCompact S210 USA) equipped with a conductivity probe (InLab 720) was used to measure the conductivity of polymer solutions. Five readings were taken for each solution at ambient temperature, and the mean value was recorded.

d_{33} meter: The piezoelectric coefficient of the electrospun fiber mat was analyzed using a d_{33} meter (YE2730A d33 meter, Sinocera, China). An Au layer of 20 nm was deposited on both sides of the mat as an electrode. The average d_{33} values were taken from five different measurements for each sample.

Piezoelectric Force Microscopy (PFM): The local piezoelectric response of single PVDF and 7 wt% rGO/PVDF fibers were examined using PFM CoreAFM (Nanosurf, Switzerland). A conductive Pt/Si coated Si cantilever (PtSiFM, nanosensors, Switzerland) with a spring constant of 1.85 Nm^{-1} and a resonance frequency of 6 kHz was used for the measurements. The topography images were acquired in static PFM mode by applying an AC voltage of 10 V between the cantilever tip and the bottom electrode. ITO was considered as a control and background for the fiber samples.

Kelvin Probe Force Microscopy (KPFM): The topography and surface potential of the individual fibers were analyzed using the KPFM mode of CoreAFM (Nanosurf, Switzerland). A conductive tip HQ:NSC18/PT (MikroMasch, Bulgaria) with a force constant of 2.8 Nm^{-1} and a resonance frequency of 75 kHz was employed to conduct the measurements. The surface topographic images were obtained from an area of 10 × 10 μm. Surface potential was computed from the average scan lines on each fiber. Seven different fibers were scanned on the separate scan regions for the statistical analysis of the data. ITO served as a control measurement for the KPFM signals.

Scanning Thermal Microscopy (SThM): The thermal analysis of the single fibers was conducted using an Atomic Force Microscope (AFM, CoreAFM (Nanosurf, Switzerland) equipped with an SThM module (VertiSense, AppNano, USA). A VTP-200 thermal probe (AppNano, USA) with a silicon cantilever with 9.9 Nm^{-1} spring constant and a hollow silicon dioxide tip integrated with a 50 nm thermocouple at the apex of the tip were used to carry out thermal scanning. The cantilever tip was heated with a laser, and the temperature gradient between the tip and the stage was set to 60℃ before coming in contact with the sample. The data was collected by performing the spectroscopy over three lines for each sample. Each line with a length of 10–20 μm was divided into 32 pixels. The tip approached and contacted the sample at each pixel and retracted. Simultaneously, the temperature on the tip was noted as the change in the thermocouple voltage. The time and amplitude for each time approach and retraction of the tip were set to 3 μm and 2 s, respectively. The amount of force as a stop-by value was 75 nN. The average temperature of the fibers was measured by taking the measurements related to pixels on the fiber where the tip was in contact with the fiber. All the measurements were performed at ambient temperature. Also, all the measurements were conducted by using the same thermal probe to evade any potential difference in thermal transport variation related to the probe. Three different fibers were selected from the various areas of the sample to conduct the measurements, and the average values were noted by considering ITO as a background for all sets of measurements.

Piezoelectric energy harvesting: The piezoelectric power generation performance of the PVDF and 7 wt% rGO/PVDF fiber mat was executed using a bespoke setup with a linear motor (LinMot – P04, USA). In order to eliminate the possible contribution from the triboelectric effect due to contact with other surfaces, we programmed the setup to apply an oscillating pressure of 0 to 40 N with a 1.5 Hz frequency. The fiber mat with a diameter of 12 mm was attached to an Al electrode using silver paste (Acheson Silver DAG 1415 M, China). The current output was measured by taking the connections from both Al electrodes using an electrometer (Keithley 6517B, Cleveland, USA). The current measurements were also evaluated against different resistors ranging from 0 to 1000 MΩ. For each sample, the measurements were taken after a 30 min. stabilization period. This allows us to obtain precise and stable output electrical measurements. The output current against all the resistors was computed by taking the peak-to-peak distance of the output current and analyzed in Origin Pro (2022, OriginLab, USA). The average current output value was calculated from 3 different tests on each sample.

Triboelectric energy harvesting: The same setup mentioned above for piezoelectric energy harvesting was used for the triboelectric measurements. The setup consists of a linear motor (LinMot-P04, USA), and it works by continuously tapping the PA6 fiber mat (triboelectric positive) against PVDF and 7 wt% rGO/PVDF (triboelectric negative). A detailed description of the electrospinning of PA6 is provided in the supporting document. The PVDF and the composite mats with 12 mm diameter were connected to an Al electrode using silver paste (Acheson Silver DAG 1415 M, China). Similarly, PA6 mats were also attached to the Al electrode using silver paste. The tapping parameters were set to 1.5 Hz and 20 N with a 20 mm distance between the PVDF and PA6 counter electrode. An electrometer (Keithley 6517B, Cleveland, USA) was used to measure the generated current output from the fiber. The current values were also noted against different resistors (0 to 1000 MΩ), and the peak-to-peak distance of the output current values was analyzed in Origin Pro (2022, OriginLab, USA). To get a stabilized and clear current value, the measurements were taken after running the experiment for 30 min. for each sample. All the presented values were an average of 3 discrete tests on each sample type.

Pyroelectric energy harvesting: The nanogenerator was made from an active layer of 15 × 15 mm of PVDF, or composite mat sandwiched between an Al foil as electrodes on both sides of the mat. A Cu tape was used to take the connection from both electrodes to measure the generated current. The nanogenerator was fixed on the table to eliminate the electrical signals coming from the movement. This helps to avoid any possible piezo or triboelectric effect. We used a hair dryer to simulate the cold and hot air flow and passed the different temperature air flows (cold: 45 ℃ and hot: 80 ℃) over the nanogenerator. The hair dryer was also fixed and kept a distance of 11 cm from the nanogenerator. The produced signals were recorded using a digital multimeter (Keithley DMM6500, USA).

3. Results and discussion

In this study, we evaluate the effect of rGO filler (1, 5, 7, 10 wt%) incorporation into the PVDF matrix to enhance the β phase, crystallinity and energy harvesting properties. A multifunctional nanogenerator was made based on rGO/PVDF composite, as shown in Fig. 1. A comprehensive study was done based on the multifunctional properties belonging to PVDF, such as piezoelectric, triboelectric, and pyroelectricity. The PVDF fibers and the PVDF/rGO composites were produced via electrospinning. The electrospun fibers quality was optimized for pure PVDF and its composites by adjusting the electrospinning parameters such as concentration of the solution, voltage, flow rate, and distance between the collector and the needle tip. The samples are labeled as 1 wt% rGO/PVDF, 5 wt% rGO/PVDF, 7 wt% rGO/PVDF and 10 wt% rGO/PVDF.

The randomly produced electrospun fiber's SEM micrographs are

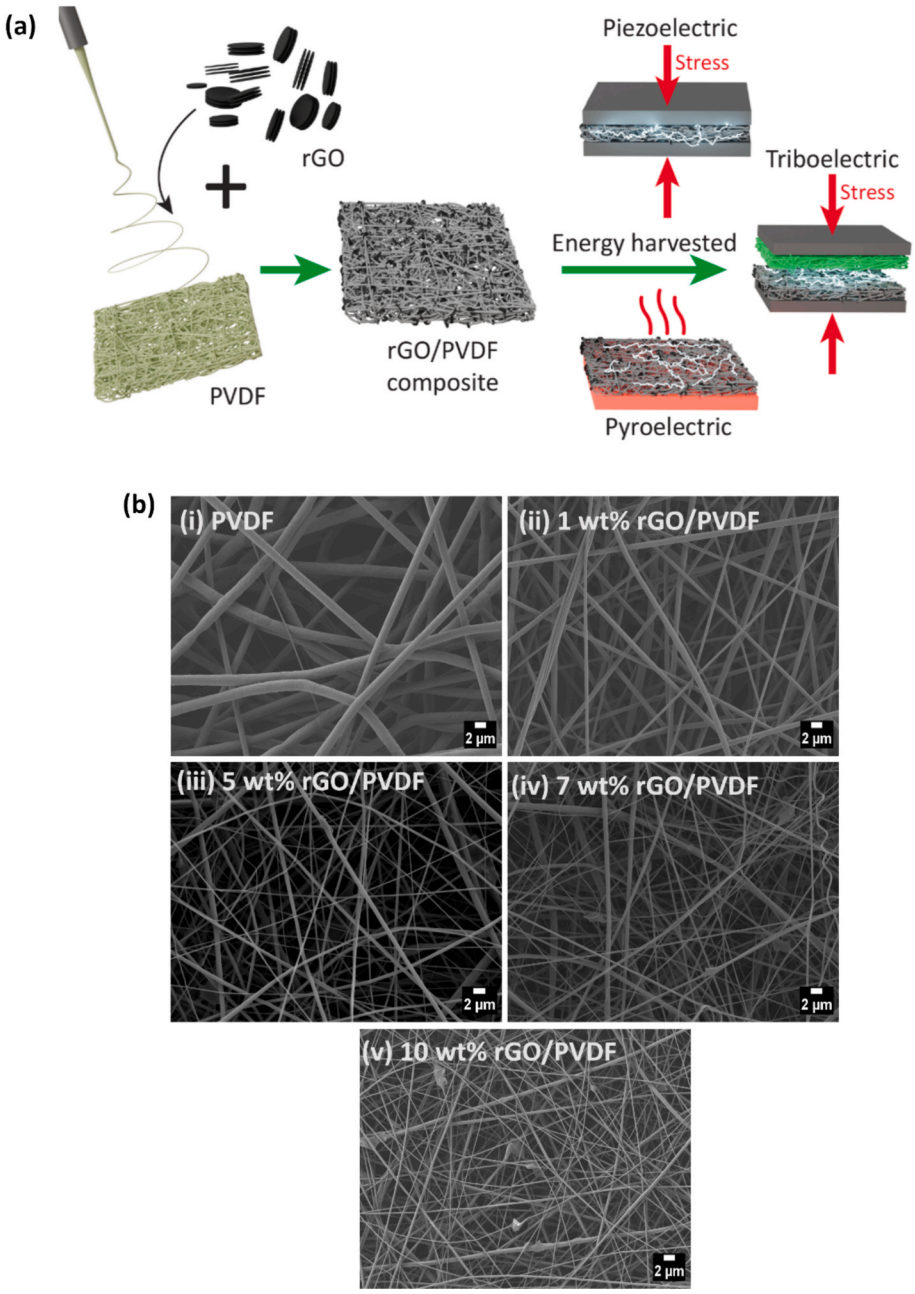

Fig. 1. (a) Schematic illustration of the multifunctional electrospun rGO/PVDF composite fiber in energy harvesting using piezo-, tribo- and pyroelectric effects. (b) SEM micrographs with higher magnification insert view (i) PVDF (ii) 1 wt% rGO/PVDF (iii) 5 wt% rGO/PVDF (iv) 7 wt% rGO/PVDF (v) 10 wt% rGO/PVDF.

presented in Fig. 1b. Uniform fibers without any beaded structure are electrospun by optimizing the parameters listed in Table S1 in the supplementary information. Fig. 2a presents the fiber diameter distribution curve of PVDF and rGO/PVDF composites. PVDF fibers have a fiber diameter of 1.51 ± 0.3 μm. It can be observed that the average fiber diameter for PVDF is significantly decreased with the presence of well dispersed rGO filler due to the increased electrical conductivity of the electrospinning solution[31]. Additionally, Fig. 2b represents the relation between the solution conductivity and fiber diameter vs rGO content (wt%). As shown, 1 wt% rGO/PVDF has a fiber diameter of 650 ± 200 nm with a solution conductivity value of 0.59 ± 0.06 μScm^{-1}. PVDF dissolved in DMAc/acetone solvents exhibits a solution conductivity of 0.13 ± 0.01 μScm^{-1}, notably 4.5 times lower than the 1 wt% rGO/PVDF solution. Moreover, the varying concentrations of rGO/PVDF (5 wt%, 7 wt%, 10 wt%) result in fiber diameters of 340 ± 154 nm, 200 ± 77 nm, and 390 ± 216 nm respectively. Correspondingly, these solutions demonstrate conductivities of 1.7 ± 0.15 μScm^{-1}, 2.09 ± 0.11 μScm^{-1}, and 3.98 ± 0.87 μScm^{-1} respectively. The increase in rGO content causes an increase in the charge density of the polymer solution at high voltage, which further generates a high elongation force on the ejected jets during electrospinning [38,44]. Therefore, due to the higher conductivity of rGO in high-weight percentage loaded samples, the fiber diameter notably reduced for each of the composite PVDF fibers. Contrary to other samples, 10 wt% rGO/PVDF shows an increase in fiber diameter. This can be explained by the fact that 10 wt% reaches the percolation threshold of rGO in the PVDF fibers. Therefore, more elongation force is applied to the rGO network than to the polymer [44]. Also, the agglomeration of rGO particles is visible in SEM images to the maximum filler loading, causing the formation of beads at a considerably high solution viscosity. Abolhasani et al. [44] found similar results in their study by preparing PVDF/graphene composites. The results revealed that adding 5 wt% graphene filler to PVDF reached the

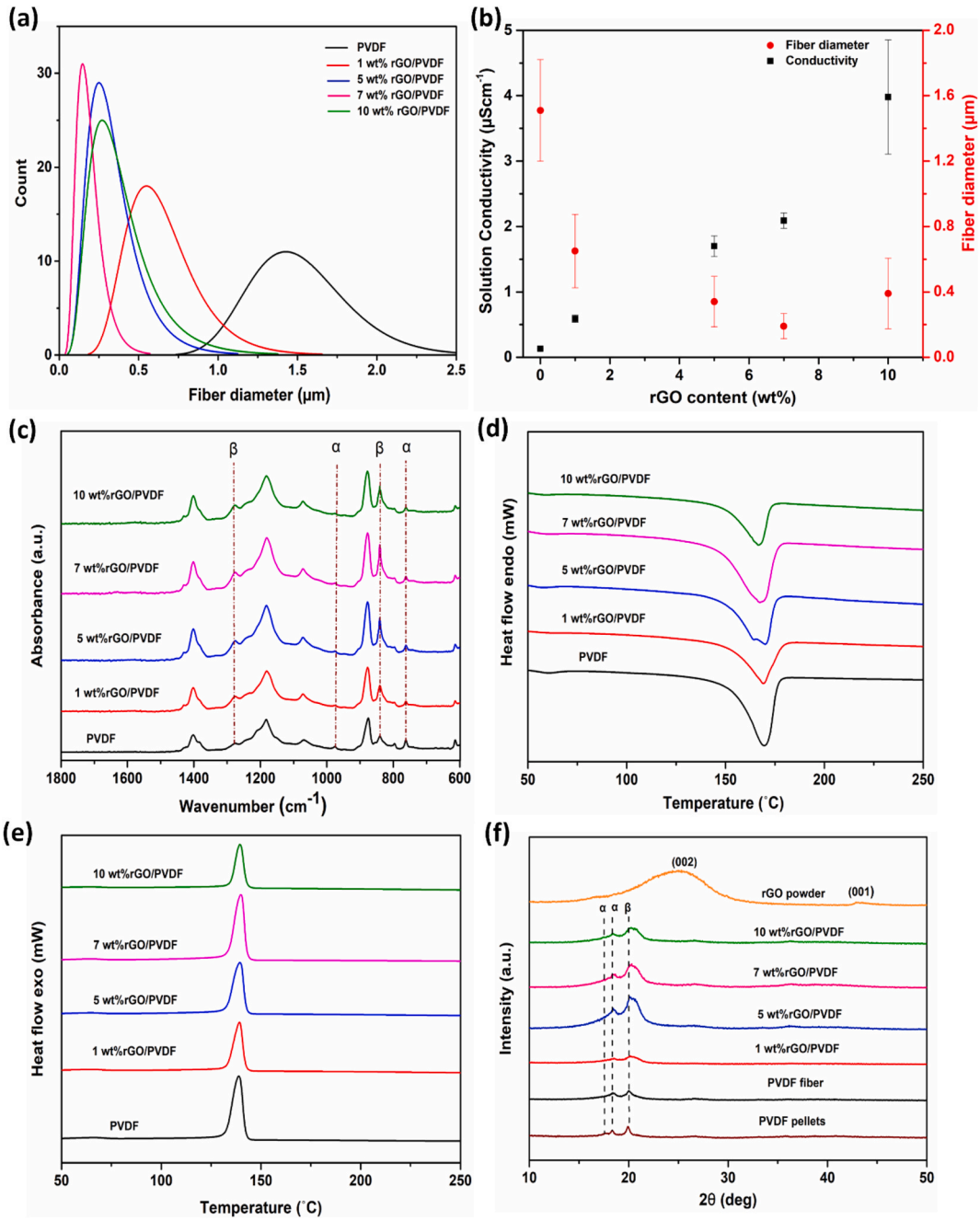

Fig. 2. (a) Fiber diameter distribution curve from PVDF and rGO/PVDF composites (b) Relationship between conductivity and fiber diameter vs rGO content in PVDF fiber (c) FTIR spectra of rGO/PVDF composites (d) DSC heating thermograms for all samples (e) DSC cooling thermograms (f) XRD diffractogram of rGO/PVDF composites.

percolation threshold and a similar phenomenon was observed that the fiber diameter increased compared to the rest of the composites due to the higher stretching of the graphene network than in the PVDF.

After producing the PVDF and composite fibers, the electroactive phases present in the samples were analyzed through FTIR. The emergence of the peaks at 613, 763, 946 cm^{-1} in the FTIR spectra (Fig. 2c) were the characteristic vibrational bands for the α phase [45,46]. The peaks at 840, 1276 cm^{-1} indicate the occurrence of the electroactive β + ϒ phase [45,47]. It is observed that the peak intensity of the β + ϒ phase phase is higher in all the rGO added composite samples than in the pristine PVDF fiber. The characteristic α phase intensity at 613, 763, and 946 cm^{-1} is prominent in PVDF fiber. While negligence or disappearance of the α peaks could be noticed for the composite samples. The equation in ref. [31] was employed to calculate the relative β phase fraction (F(β)) in PVDF[31,45]. Compared to PVDF, the β phase fraction in rGO composite fibers was increased (Table S2, supplementary information). The intensity of the absorption band peak that appeared at 840 cm^{-1} increased with the incorporation of a small amount of rGO (1 wt %). Therefore, β phase content rose to 69 % compared to the pristine PVDF fiber, which had 60 % of β phase. For 5 wt% rGO/PVDF, a sharp β + ϒ phase absorption band is present, and the β phase fraction reached 78 %. That is, beyond specific filler concentration (above 1 wt%), the β + ϒ phase intensity becomes prominent, and thus, the β phase content also shows a significant increase. This means that the β + ϒ phase stability became more prevalent with increased rGO loading into the PVDF matrix. Further increasing the filler loading to 7 wt% showed a sharp

absorption peak at 840 cm^{-1} (β + ϒ phase), with a higher peak intensity than 5 wt% rGO/PVDF. The β phase faction of 7 wt% and 10 wt% rGO/PVDF are 81, and 79 %, respectively. This increase in β + ϒ phase faction can be described as follows; rGO served as a nucleating agent and stimulated the nucleation of crystalline PVDF β phase through solid interactions at the interface. Moreover, the conductive rGO leads to an increased charge due to the increase of the local electric field. This causes a formidable coulombic force and attracts the PVDF segments to crystallize into the β phase [44,48]. As a result, the content of the β + ϒ phase in composites increased compared to pristine PVDF fibers. However, for 10 wt% rGO/PVDF the β phase fraction is decreased compared to the 7 wt% rGO/PVDF. Because 10 wt% rGO was above the percolation threshold of rGO in PVDF, this led to an agglomeration of particles inside the PVDF fibers, and the fiber diameter increased as described in SEM analysis.

Thermal analysis was performed using differential scanning calorimetry (DSC) to perceive different phases of crystalline forms of PVDF and to investigate how rGO affects the crystallization and melting behavior of PVDF electrospun fibers. Fig. 2 d and e illustrate the endothermic and exothermic DSC curves of PVDF and PVDF/rGO composites. DSC results, including the melting temperature (T_m), melting enthalpy (ΔH_m), and crystallinity content (χ_c) of all the samples, are summarized in Table S2 (supplementary information). All the samples' crystallinity contents (χ_c) were calculated using the equation from the previous studies [31]. From Fig. 2 (d), all the composites showed increased crystallinity. The melting peak at 167–170 °C refers to the combined α and β phase peaks [49,50].

DSC is not an appropriate tool to distinguish the α and β phases in PVDF as the β crystallites show a similar melting temperature to those of the α phase [50–52]. However, DSC is used to calculate the percentage of crystallinity of PVDF [52]. The crystallinity increased from 44.05 % for the pristine PVDF fibers to 46.89 %, 47.03 %, 48.01 %, and 46.09 % for the rGO/PVDF composites with 1 %, 5 %, 7 %, and 10 wt% rGO content, respectively. Aligned with the FTIR results, the crystallinity of 10 wt% rGO is reduced compared to the other composite samples. Fig. 2e shows a slight crystallization temperature (T_c) increment for composite fibers compared to the pristine PVDF. Incorporating 1, 5, 7, and 10 wt% rGO into PVDF has displayed a crystallization temperature of 139.09, 139.93, 139.91, 139.50 °C. In comparison, PVDF showed a T_c of 138.83 °C. The rise in T_c indicates that the rGO acts as a nucleating agent for the crystallization of PVDF. This is due to the high surface area of rGO and the interactions between rGO and PVDF [38]. The decrease in crystallization temperature and crystallinity at higher rGO content (10 wt%) is due to the lesser interaction of rGO in the PVDF matrix due to the agglomeration of the rGO particles and the beaded structure.

XRD diffractometry was executed to determine further α and β phases present in PVDF and the rGO/PVDF composite. Fig. 2 f shows the XRD results obtained from pure PVDF pellets, electrospun PVDF and composite fibers, and the rGO powder samples. The characteristic peak of rGO is visible at 24.10° 2θ corresponds to the (002) plane, and a low intensity peak can be observed at 42.60° 2θ with (001) plane orientation [37,53]. From the XRD pattern, the PVDF fibers appear to possess β and α phases. PVDF pellets mainly have the α phase with a characteristic diffraction peak observed at about 2θ = 17.6° (100), 18.5° (020), 26.56° (021) and 39° (002) [54,55]. Electrospun PVDF fibers show diffraction peaks at 18.5° (α phase) and a sharp peak around 20.5° 2θ, which signifies the sum of the diffractions at (110) and (200) planes for the characteristic β phase [54,56]. Furthermore, the characteristic peaks assigned for the α phase at 17.6° completely disappeared, and negligence and weakening of the peaks at 18.5° and 39° 2θ are discerned for the PVDF fibers and their composites. This again confirms that electrospinning helps to improve the piezoelectric properties of PVDF by enhancing the conversion of α phase into β phase owing to the stretching of the polymer jet at high voltage applied during the electrospinning [38,54]. Moreover, higher weight percentage loading of rGO to the PVDF matrix causes an intensification of the β phase (20.5° 2θ) compared to the electrospun PVDF. The incorporation of the lowest amount (1 wt%) into PVDF started to indicate the significant effect of rGO by increasing β phase intensity at 20.5° and lowering the intensity of α phase at 18.52θ. Compared to 1 wt% rGO/PVDF, the β phase intensity is twice as high for 5 wt%, 7 wt% rGO/PVDF composites. Hence, the XRD results again prove that rGO greatly enhances the β phase intensity. This β phase increment in the composite is owed to the surface charge of rGO, which interacts with the $–CH_2–/–CF_2–$ dipoles of PVDF [35]. That is the development of electrostatic interaction between rGO and PVDF matrix [37,57]. For 10 wt% rGO/PVDF, the β phase intensity is diminished compared to 5 and 7 wt% rGO/PVDF composites, supported by FTIR and DSC results. That is, above the percolation threshold, beaded structure formation occurs due to the high viscosity of the solution. Furthermore, no characteristic peaks from rGO could be observed for the PVDF composites even with the higher addition rGO, and this may be due to the shifting of the peak position of rGO during the interaction with PVDF.

Further, the piezoelectric coefficient (d_{33}) was measured to verify the piezoelectric response of the fiber mats. The d_{33} value for pristine PVDF was 7 ± 0.2 pCN^{-1}, whereas the composite samples displayed an increase in d_{33} values. 1, 5, 7 and 10 wt% rGO/PVDF has obtained a d_{33} value of 11.2 ± 0.2, 15.1 ± 0.5, 16.9 ± 0.2, 14.7 ± 0.4 pCN^{-1} respectively. The results confirm that 5 and 7 wt% rGO/PVDF composites showed the highest β phase and crystallinity, and thereby, high piezoelectric response. Additionally, the porosity of electrospun fiber is approximately 90 % [58]. Therefore, the d_{33} value might not be as high as the PVDF films [31].

The FTIR, DSC, XRD and d_{33} studies suggest the enhancement in β phase, crystallinity and piezoelectric coefficient in electrospun fibers in the presence of a higher weight percentage of rGO (5 wt% and 7 wt%) incorporation into PVDF. This would make them a suitable candidate for fabricating a multifunctional nanogenerator with combined piezoelectric/triboelectric/pyroelectric properties. From the above characterization studies, we can conclude that 7 wt% rGO/PVDF composite exhibits the highest β phase content (81 %) and crystallinity (48.58 %). Therefore, to further investigate the applicability of rGO/PVDF composite in piezo/tribo/pyroelectric properties, we have chosen the 7 wt% rGO/PVDF and PVDF fiber as a reference sample.

3.1. *Piezoelectric characterization*

In this section, we investigate and compare the piezoelectric response of PVDF and 7 wt% rGO/PVDF fiber at the micro and macroscopic levels. Under the PFM mode, the electromechanical response of the fiber was examined using the converse piezoelectric effect [59]. PFM allows us to measure the local piezoelectric response regarding amplitude and phase signals [59,60]. AC voltage was applied to the selected single fibers, which induced structural deformation [61] and the signal was detected and acquired through a lock-in amplifier. In this measurement, a 10 × 10 μ m^2 fiber area was scanned. The topographic images of PVDF and 7 wt% rGO/PVDF fiber are shown in Fig. S1(a) and (b) in the supplementary information (SI). The results support the SEM images that the 7 wt% rGO addition drastically changes the fiber diameter due to the highly electrically conductive nature of rGO [31,58]. Fig. 3a and b show the PFM phase signals from PVDF and 7 wt% rGO/PVDF fiber, indicating the polarization orientation. The phase images of the fibers display the antiparallel piezoelectric domain switching with a 180° domain wall [62]. The images in Fig. 3c and d represent the PFM amplitude signals from PVDF and 7 wt% rGO/PVDF fiber, corresponding to the piezoelectric displacement. The amplitude images reveal a pronounced piezoelectric contrast due to the deflection created by the applied AC field [60,61]. Fig. 3e gives the average PFM amplitude results obtained from five different individual fibers (the complete data from the individual fibers are included in the supplementary Information Fig. S1 (c)). The amplitude values for ITO, used as the background were similar, 2.13 ± 0.87 pN and 5.67 ± 0.44 pN from

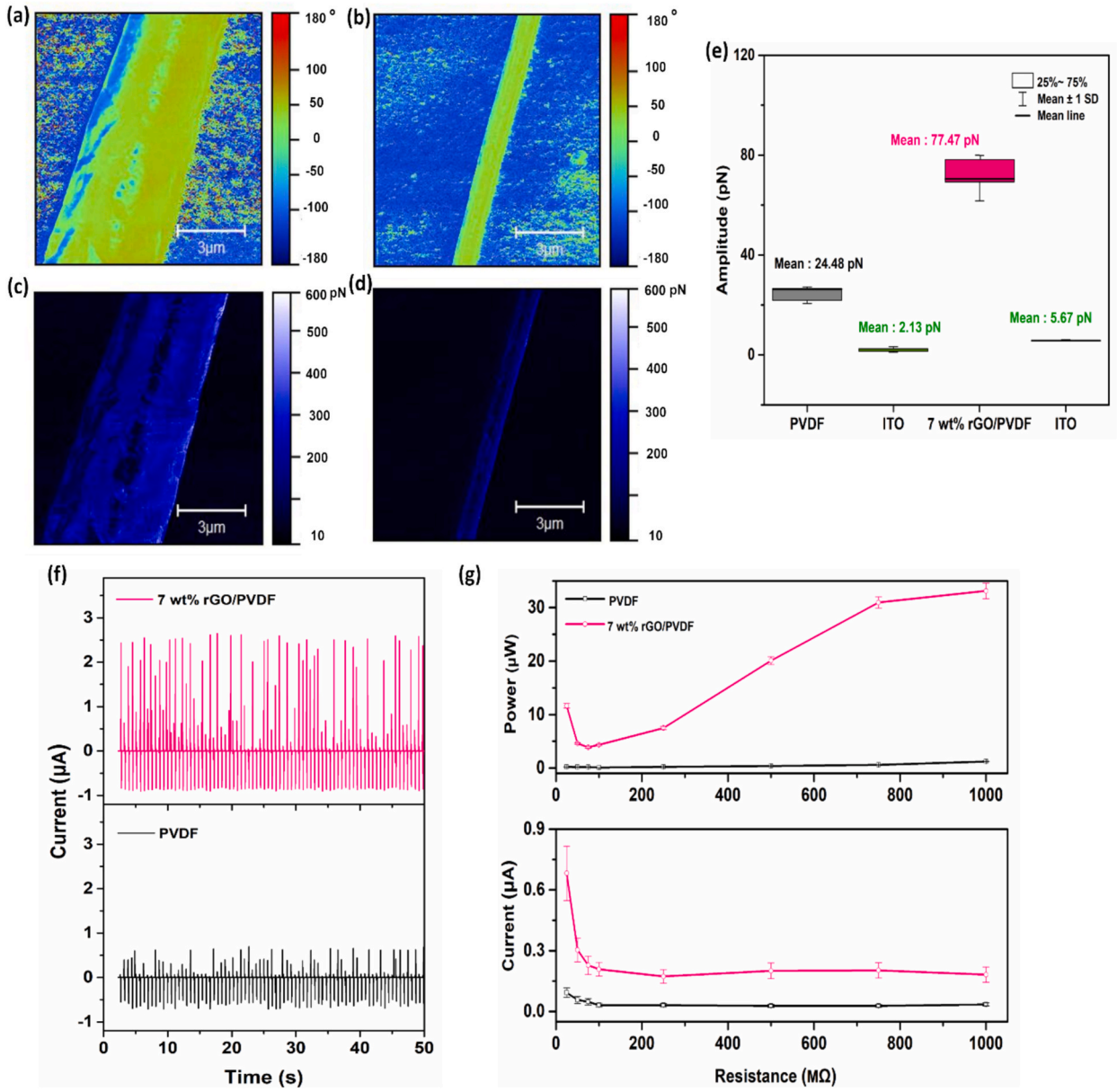

Fig. 3. PFM and piezoelectricity measurements from PVDF and 7 wt% rGO/PVDF (a) Phase map of PVDF (b) Phase map of 7 wt% rGO/PVDF (c) Amplitude map of PVDF (d) Amplitude map of 7 wt% rGO/PVDF (e) average amplitude graph of individual fibers of PVDF and 7 wt% rGO/PVDF (f) piezoelectric current vs time of PVDF and 7 wt% rGO/PVDF (g) Current and power measurements of PVDF and 7 wt% rGO/PVDF across different resistance from 25 MΩ to 1000 MΩ.

PVDF and composite fibers, respectively. PVDF fibers show a PFM amplitude of 24.48 ± 3.09 pN, and 7 wt% rGO/PVDF fibers have an increased amplitude of 77.47 ± 17.88 pN. Therefore, the results indicate that 7 wt% rGO enhanced the PFM amplitude three times more than the pristine PVDF fibers. Hence, 7 wt% rGO/PVDF has a higher piezoelectric response due to the improved β phase content and crystallinity.

The electromechanical response of the individual fibers from PFM data again proved that the piezoelectric response is improved in the presence of rGO for electrospun PVDF fibers. Thus, it is possible to use this material as a PENG in energy harvesting applications to convert the vastly available mechanical energy into electrical energy. The piezoelectric response of the 7 wt% rGO/PVDF mat was examined using a periodic pressing and releasing of the sample using a linear motor system without any tapping to eliminate the triboelectric effect. The output piezoelectric current was recorded using a digital multimeter by applying a loading force of 40 N under a frequency of 1.5 Hz. A schematic diagram showing the piezoelectricity testing setup is shown in the supplementary Information Fig. S1d. The load characteristic of the PENG was determined by measuring the current under various resistances from 25 MΩ to 1000 MΩ, using the same parameters mentioned above.

The working mechanism of PENG is illustrated in Fig. S1d in the Supplementary Information. When the PENG is subjected to mechanical stress, it causes a change in the orientation of dipoles, and a difference in piezoelectric potential is created between the two electrodes. In order to nullify the developed piezoelectric potential, the free charges start to move from one electrode to another, leading to a positive signal. With the immediate release of force, the accrued charges drift back in the reverse direction owing to the fading of the electrical potential and the appearance of a negative signal [2,31].

Fig. 3f shows the produced output current from PVDF and 7 wt% rGO/PVDF PENGs without any load resistance (0 MΩ). PVDF produced an output peak-to-peak current of 0.63 ± 14 μA, though the current increased to 2.4 ± 0.44 μA for the composite with 7 wt% rGO (Fig. 3f).

That is, a high amount of rGO loading positively influences the improvement of the piezoelectric output of PENG [38,63]. The piezoelectric performance enhancement could be explained as follows: rGO favored the nucleation of β phase, crystallinity as described in FTIR, DSC, and XRD sections. Further, the increase in rGO addition into the polymer matrix provides a conductive network, accelerating the transfer of the induced charge created in the composite [38,63]. Another advantage of using rGO is that less functional groups are attached to the carbon atoms in the structure of rGO [37].

Therefore, the movement of electrons is at a high speed across the carbon atom, which leads to the increased electrical properties of rGO/PVDF [37,38]. Fig. 3g demonstrates PENG's current output and power density plotted across different resistors. According to Ohm's law, the current decreased with increased load resistance for both PVDF and 7 wt % rGO/PVDF composite PENGs. For the output power and power density calculation, PVDF PENG exhibited an increased output power with increasing load resistance up to 1000 MΩ and reached a power of 1.22 ± 0.05 μW and a power density of 1.07 ± 0.04 μWcm$^{-2,}$ respectively. 7

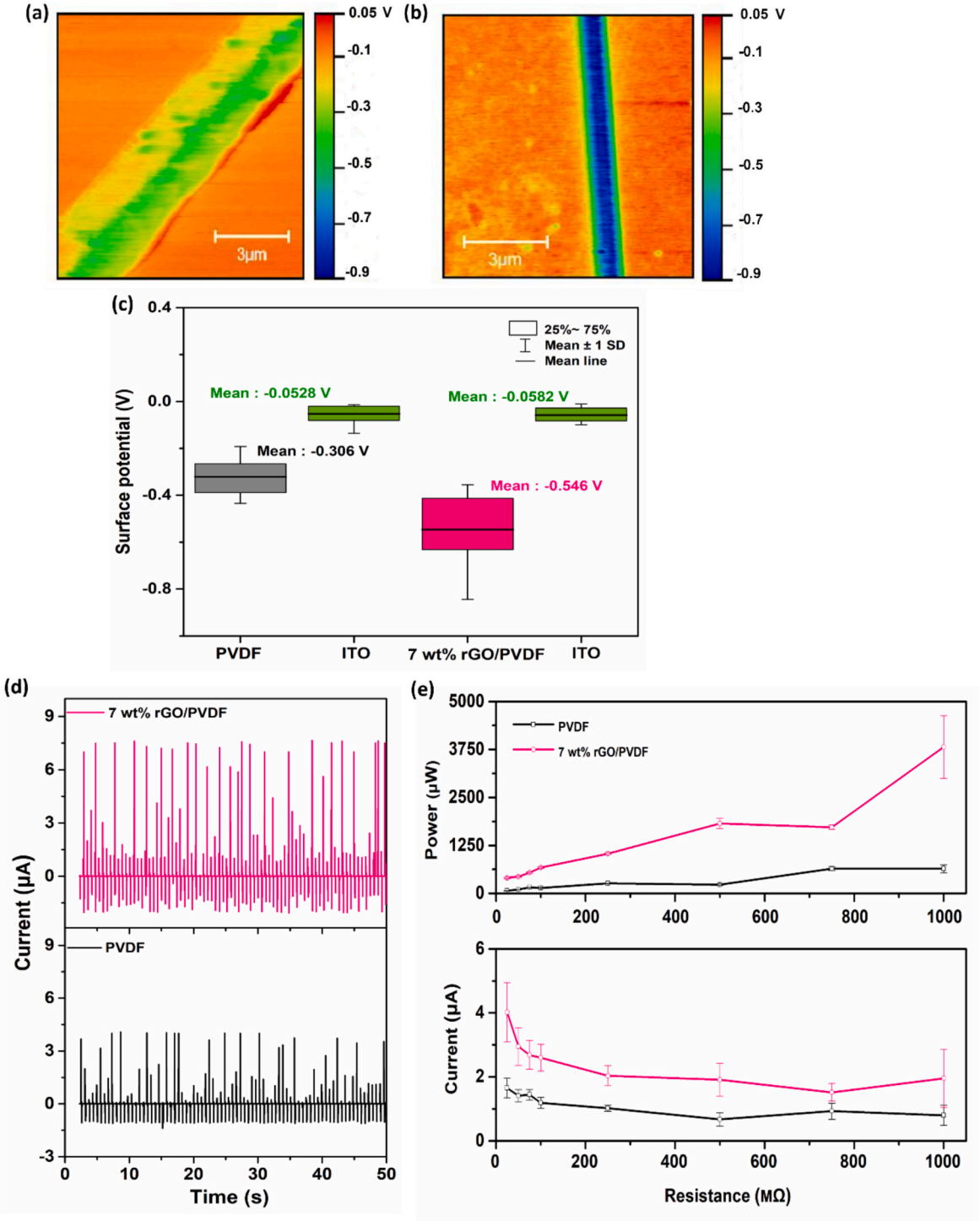

Fig. 4. KPFM and triboelectric measurements from PVDF and 7 wt% rGO/PVDF (a) surface potential map of PVDF (b) surface potential map of 7 wt% rGO/PVDF (c) average surface potential graph of individual fibers of PVDF and 7 wt% rGO/PVDF (d) triboelectric current vs time of PVDF-PA6 and 7 wt% rGO/PVDF-PA6 (e) Current and power measurements of PVDF-PA6 and 7 wt% rGO/PVDF-PA6 across different resistance.

wt% rGO/PVDF generated a maximum power and power density of 33 ± 1.43 μW and 29 ± 1.26 μWcm^{-2} at 1000 MΩ, as shown in Fig. 3g.

The durability and stability of PENG for a long-time practical application were proved by running experiments for more than 1900 cycles across all the resistance measurements. The results confirm no considerable fluctuations after more than 1900 cyclic pressing and releasing cycles. This shows the stability of the PENG prepared for real-life applications.

3.2. Triboelectric characterization

A detailed study based on the surface potential from the single fiber and the macroscopic electrostatic response from the electrospun mats was quantitatively analyzed in this section. We measured the surface potential of PVDF and the composite with 7 wt% rGO-loaded individual fibers using KPFM. This helps to verify how rGO incorporation into the PVDF matrix affects and changes the surface potential of the composite material. KPFM is a key tool to measure the contact potential difference (V_{CPD}). During the measurement, an alternating current (AC) voltage is applied to the cantilever, which induces an electrostatic force between the tip and sample and is detected by a lock-in amplifier. A lock-in amplifier detects this force. Subsequently, a direct current (DC) voltage is employed to counterbalance the potential, thereby preventing the cantilever's oscillation. This DC voltage is then utilized to quantify the contact potential difference between the tip and sample [18,64,65]. Fig. S2 a and b (supplementary Information) shows the topographic images of PVDF and 7 wt% rGO/PVDF fiber with a scanning area of 10 × 10 μm^2. It shows the normal fiber morphology with decreased fiber diameter for the composite with rGO inclusion. Fig. 4 a, b, and c represent the surface potential maps and the corresponding average surface potential graph of PVDF and 7 wt% rGO/PVDF, respectively. The data shows that the surface potential gradually decreased for the composite fibers, and the surface potential of ITO is stable for both samples. The average surface potential value of PVDF was −0.306 ± 0.129 V, whereas 7 wt% rGO/PVDF exhibited a value of −0.546 ± 0.238 V. The complete data from seven individual fibers from different parts of the sample are included in the supplementary Information Fig. S2 (c). Composite fiber had almost double the negative potential of the surface compared to pristine fibers. For both samples, PVDF and 7 wt% rGO/PVDF, the surface potential of ITO is −0.0528 ± 0.043 and −0.0582 ± 0.032, respectively (Fig. 4c). The decrease in negative surface potential of 7 wt% rGO/PVDF composite is ascribed to the oxygen and hydroxyl functional groups on the basal planes and edges of rGO [65]. This enhances the electronegative potential of the polymer surface, making it effectively suitable to use as an electronegative material for triboelectric energy generation.

The KPFM results reveal that adding a higher weight percentage of rGO into electrospun PVDF fibers significantly enhances electronegativity. This implies that the position of PVDF on the triboelectric series can be tuned by adding the 7 wt% rGO. The 7 wt% rGO/PVDF with decreased surface potential can be placed on the more tribo-negative side of the series. Therefore, composite fibers can improve triboelectric properties. Further, to evaluate the triboelectric performance of the prepared composite fibers, a TENG was fabricated. The TENG comprised two parts; one part consisted of a PA6 electrospun mat acting as a triboelectric positive material. The other part was a 7 wt% rGO/PVDF mat as a negative triboelectric material. Al foil was used as an electrode for both the triboelectric parts. PVDF-PA6 TENG was also fabricated as a reference to comparing the results from 7 wt% rGO/PVDF-PA6 composite. The triboelectric performance of the TENG was evaluated using a bespoke setup with a linear motor (see Fig. S2d, supplementary information), and a force of 20 N with a frequency of 1.5 Hz was applied. The generated current output of PVDF-PA6 and 7 wt% rGO/PVDF-PA6 TENG is displayed in Fig. 4 d. The results revealed that the TENG can generate high power output. Fig. S2d in the supplementary Information shows TENG's working mechanism in contact separation mode. Initially, the triboelectric materials are separated from each other and have no charge. During the application of an external force, the 7 wt% rGO/PVDF mat comes into contact with the PA6 fiber mat. According to the triboelectric effect, an equal amount of opposite charge transfer occurred at the contact interface between the 7 wt% rGO/PVDF and PA6 due to the varying electron affinities. When both materials are in contact, PA6 a tribopositive material tends to give out electrons and acquire a positive charge [64]. PVDF, as a tribonegative material, attracts the electrons from PA6, resulting in a negative charge on the 7 wt% rGO/PVDF mat surface. With the release of the external force, an electrical potential is created, causing the charge to flow from the bottom electrode to the top electrode, thereby equalizing the potential difference. Through continuous release, the bottom electrode (7 wt% rGO/PVDF) maintains a positive charge comparable to the negative charge on the 7 wt% rGO/PVDF mat due to electrostatic induction. The balance of electrostatic induction is disrupted upon applying an external force, and the electrons migrate backwards from the top electrode to the bottom electrode. Therefore, by cyclic compression and releasing, an alternating current is generated due to the oscillation of electrical potential difference between the electrodes [3,64].

The generated output current measurement across different resistors from 0 to 1000 MΩ from the TENG was recorded. A stable output current was observed for all the experiments. The dependency of output on load resistance was characterized by PVDF-PA6 and 7 wt% rGO/PVDF-PA6 TENGs in terms of current output and power, as displayed in Fig. 4e. The TENG produced the highest output current of 4 ± 1 μA and 7.2 ± 2 μA for PVDF-PA6 and 7 wt%rGO/PVDF-PA6, respectively. Further increasing the load resistance showed saturation of current. This can be explained as follows. At zero external resistance (short circuit), the circuit allows for maximum current flow theoretically, but in the case of a TENG, the internal impedance of the generator limits the actual current that can flow. TENGs typically have a relatively high internal impedance [66,67]. With a short circuit, most of the generated charge remains trapped within the device, leading to a low effective current. As the load resistance increases from zero, it begins to approach the internal impedance of the TENG. At this point (around 250 MΩ), the circuit impedance matches more closely, allowing for a more efficient transfer of charge from the triboelectric device to the load. This optimal matching between the internal impedance of the TENG and the external resistance maximizes the current output because the voltage across the load is sufficient to drive more charge through the circuit [66,68]. When the resistance increases beyond the optimal point, the circuit's total resistance becomes too high. According to Ohm's law, the current decreases because the higher resistance limits the flow of charge [66,67]. The power output from the TENG was calculated. The results demonstrated a linear increase in power output with increasing load resistance, and the highest power was achieved at the resistance of 1000 MΩ. PVDF-PA6 TENG showed a power output of 641 ± 99 μW, which increased to 3812 ± 813 μW for the 7 wt%rGO/PVDF-PA6. Similarly, the power density was noted for PVDF-PA6 and 7 wt%rGO/PVDF-PA6, are 567 ± 87 μWcm^{-2} and 3373 ± 719 μWcm^{-2} respectively. Hence, these results confirm that the inclusion of rGO into PVDF can substantially improve the triboelectric performance of PVDF, which is in accordance with the results from the KPFM data (Fig. 4c). The negative surface potential is increased by 7 wt% rGO/PVDF compared to pristine PVDF because rGO acts as a charge-trapping site in the PVDF matrix. This expands the interface potential for charge storage. During friction, the attracted electrons from PA6 are stored or trapped in rGO particles. Thereby, it enhances the composite's surface charge and slows the charge's dissipation [69]. For each measurement, a stable triboelectric output was obtained from the repeated tapping and releasing movement for more than 1900 cycles for the TENG. This indicates the reliability and durability of the TENG for practical applications and integration into smart textiles for energy generation.

By comparing the piezoelectric and triboelectric power output from PVDF and 7 wt% rGO/PVDF, we can conclude that the higher

percentage of rGO has remarkably improved the output performance of the nanogenerator. However, 7 wt% rGO/PVDF-PA6 TENG delivered a higher power density of 3373 ± 719 μWcm^{-2}, which is more than 115 times higher than the 7 wt% rGO/PVDF PENG (29 ± 1.26 μWcm^{-2}). This result suggests that proper elimination of the triboelectric effect is required to differentiate the tribo and piezoelectric effect from the nanogenerators. Therefore, the higher contribution of power enhancement mostly comes from the triboelectric effect in PENG. Calavalle et al. [70] studied the electromechanical and electrostatic response of P(VDF-TrFE) single nanofibers using PFM and KPFM. The results from their studies disclosed that electrospinning promotes the growth of the β phase in the polymer and is responsible for the piezoelectric properties. The PFM data showed that the applied electric field is insufficient to induce direct ferroelectric domain polarization. However, the KPFM results explain the accumulation of triboelectric surface charges and trapped charge present in the polymer. This result agrees with our findings that the triboelectric output is superior to the piezoelectric output from the 7 wt% rGO/PVDF composite fibers. Rana et al. [12] fabricated a piezo-tribo hybrid nanogenerator based on boron/nitrogen-codoped rGO/PVDF film. The authors reported that the PVDF/BN-rGO hybrid structure showed better electrical performance due to the synergistic effect of piezo and triboelectric effect. However, comparing the electrical performance of the PVDF/BN-rGO, the TENG showed a higher output current and voltage than the PENG. The authors also demonstrated the energy stored in the capacitor, which is ~ 4.5, 20.4, and 28.8 μJ for PENG, TENG, and hybrid nanogenerators. These results again proved that the triboelectric effect is more pronounced to enhance electrical performance.

3.3. Pyroelectric characterization

To demonstrate the different interchangeable properties of the prepared composite device and their applicability, we introduced the thermal energy harvesting performance of the composite in this section. The thermo-electric energy conversion of the prepared composite was done based on the pyroelectric effect. PVDF is a pyroelectric material that can convert temperature fluctuations into electrical power [27]. Therefore, cyclic cooling and heating of the pyroelectric material offers a way to convert the waste heat into electricity [19]. Also, the temperature response can be enhanced by creating a thermally conductive network to increase the heat transfer [25]. As rGO is a thermally conductive filler [39], we analyzed the effect of thermal conductivity and heat transfer of single fibers using Scanning Thermal Microscopy (SThM).

Using SThM's thermal conductivity contrast mode, the cantilever is heated up to the desired temperature by the AFM laser. A thermocouple is used to monitor the temperature at its tip. The temperature gradient between the tip and the stage was set up to 60 ℃ for the measurements. The test was carried out following an already-established SThM measurement protocol [71]. The temperature can be adjusted by altering the

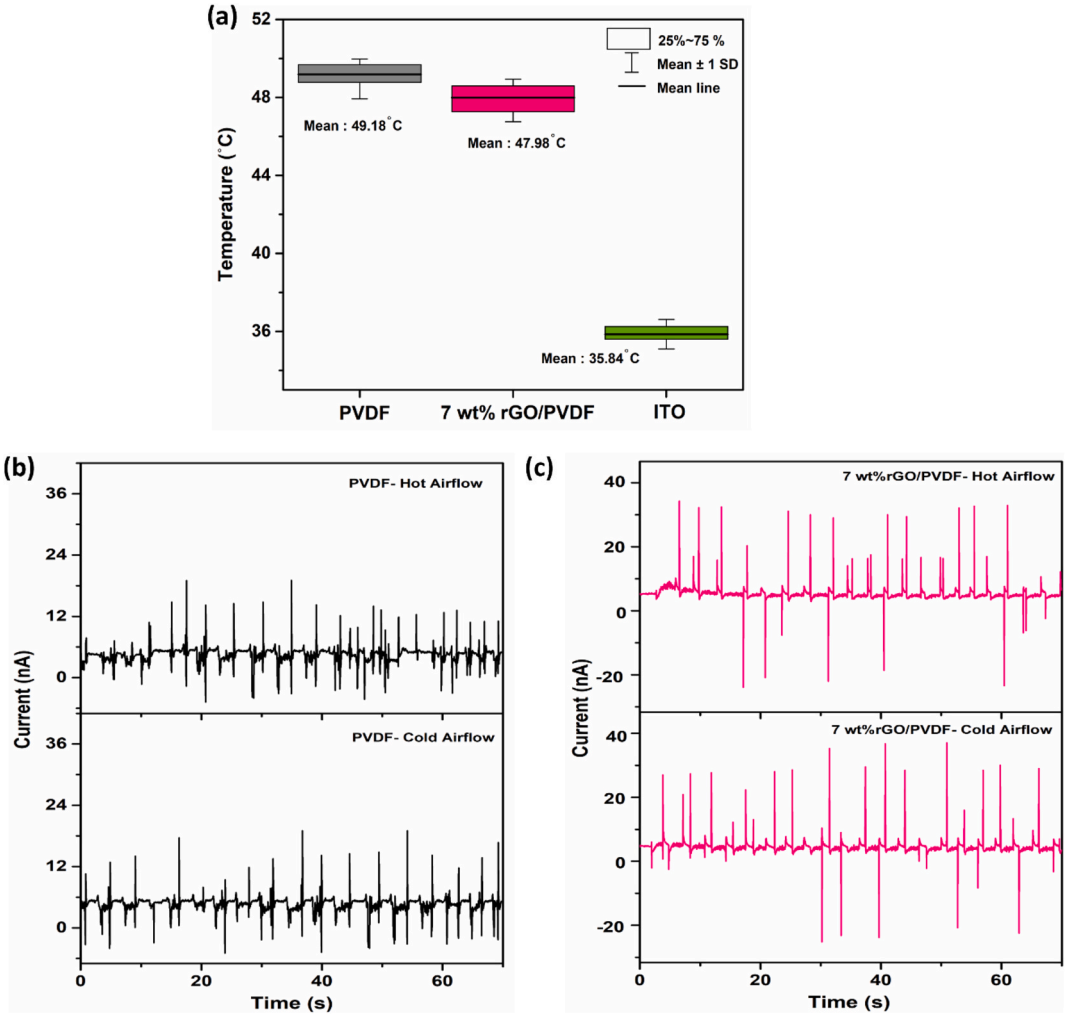

Fig. 5. (a) The average temperature of individual fibers of PVDF and 7 wt% rGO/PVDF (b) Output current from PVDF with cold and hot airflow (c) Output current from 7 wt%rGO/PVDF by cold and hot airflow.

laser position on the cantilever. The process involves a raster scanning of the tip across the sample, simultaneously measuring the temperature of the tip and generating a map that integrates thermal data with the surface features of the sample. SThM is an effective tool for probing the local thermal phenomena at the nanoscale [71]. However, it does not offer a material's quantitative thermal conductivity values. Nevertheless, the thermal distribution map provides information regarding the thermal conductivity of the scanning region. The regions of the sample with higher thermal conductivity have increased heat dissipation between the tip and the sample, resulting in a reduced temperature at the tip. Fig. 5a represents the average temperature from the single fibers and the ITO substrate as a reference material. ITO possessed an average temperature of 35.84 ± 0.42 ℃. For PVDF fibers, the tip temperature was 49.18 ± 0.79 ℃. However, it was observed that the tip temperature decreased to 47.98 ± 0.83 ℃ for the composite fiber. Hence, it confirms that 7 wt% rGO inclusion into the PVDF fiber increases thermal conductivity.

SThM results in Fig. 5a showed an increased thermal conductivity of the composite fiber and led to an enhanced heat transfer of the polymer in the presence of rGO. This makes the composite suitable for fabricating a pyroelectric nanogenerator (PyNG). Therefore, pyroelectric energy harvesting was conducted to demonstrate the multifunctional applicability of the prepared 7 wt% rGO/PVDF composite fiber. PVDF and 7 wt % rGO/PVDF PyNG were prepared and subjected to cyclic cooling and heating of the PyNG by passing cold and hot airflows. To mimic the cold and hot airflows, we used a hair dryer and flowed the cold air (45 ℃) and hot air (80 ℃) over the PyNG periodically (switching the hair dryer on and off). Fig. S3 in the supplementary information provides the schematic diagram of the pyroelectric testing setup. The PyNG was fixed on a table, and the hair dryer was also fixed above the PyNG. This helps to avoid the electrical signals generated from the movements. Fig. 5b displays the output current generated from the PVDF in the cold and hot airflows. During the cold and hot airflows, PVDF produced an output current of 18nA and 19nA, respectively. The result indicates that, according to equation (1)[72], there is no increase in pyroelectric current (I_p) with the rate of temperature change (dT/dt).

$$I_p = pAdT/dt \quad (1)$$

where p is the pyroelectric coefficient, and A is the effective area. Similar trends were obtained for 7 wt% rGO/PVDF composite with an output current of 32 and 33 nA from the periodic cold and hot airflows, respectively. This result suggests that we cannot accurately harvest pyroelectric current from the device due to the very low pyroelectric current produced from the temperature variation, which probably overlapped with the triboelectric current that was created due to the airflow. Literature studies also reported a low pyroelectric output from PVDF and its composite [24]. Li et al. [73] prepared electrospun PVDF/ZnO composite fibers, and the pyroelectric test was carried out by placing the prepared device on a flexible commercial polyimide heater. They have acquired a pyroelectric effective current of 0.8 and 2nA from PVDF and PVDF/ZnO composite, respectively. You et al. [74] fabricated a self-powered non-woven nanogenerator composed of thermoplastic polyurethanes (TPU) nanofiber membrane substrate, carbon nanotube bottom electrode, PVDF nanofiber membrane and poly (3,4-ethylene dioxythiophene): poly (styrene sulfonate)-polyvinyl pyrrolidone (PEDOT: PSS-PVP) conductive NFM (CNFM). The NG was attached to the surface of a flexible polyimide heater to convert thermal energy. Heating the NG from 313 to 319 K, an output current of 20nA and an opposite current of -16nA was observed when the temperature was restored to 313 K. From the study, they have also proved the linear increase in output current with increasing the rate of temperature change. These results also demonstrate a very low output current from pyroelectric measurements. Moreover, the linear increment in current (I_p) is very low with increasing temperature. In these cases, we also need to consider the other effects that may influence the results. Whether this increment arises from temperature fluctuation or the piezo/tribo contribution due to movement and contact, another essential factor called "thermally stimulated currents (TSCs)", that is, the release of trapped charges during the thermal excitation, may also misinterpreted as false pyroelectric current signal [75]. This is more affected in polymers and thin films since they can trap larger amounts of charges for a long time [75]. Therefore, the electrical signals generated by thermal energy harvesting must be studied in detail.

Hence, from the pyroelectric characterization, we can conclude that, due to the slight variation in generated current from the temperature fluctuation and the TSCs effect, it is difficult to state the pyroelectric effect. However, Fig. 5b and c showed a significant current enhancement for 7 wt%rGO/PVDF compared to PVDF fiber. This might be due to the contribution of the triboelectric effect.

3.4. Output performance of the 7 w% rGO/PVDF composite based TENG

Verifying the different energy harvesting performances of PVDF/rGO composite fiber indicates that the TENG power output is significantly higher than the PENG output (Fig. 6a). Hence, we have selected a 7 wt% rGO/PVDF composite to demonstrate further the device's practical applicability using triboelectricity. A comparison graph showing the output current from different PENG, TENG and PyNG from the literature and this work was illustrated in Fig. 6b. Yang et al. [38] compared the piezoelectric energy harvesting performance of GO/PVDF and in-situ reduced rGO/PVDF electrospun composites. Their results showed improved piezoelectric properties for 2 wt% rGO/PVDF than 2 wt%GO/PVDF due to the higher electrical conductivity of rGO. Also, 2 wt% rGO/PVDF PENG generated a power density of 0.0037 $mWcm^{-2}$. Ramasamy et al. [76] fabricated a phenyl-isocyanate functionalized GO/PVDF electrospun nanofiber and produced an output current of 2.28 μA and a power density of 0.0032 $mWcm^{-2}$. However, they have used an amplifier in their experimental setup to measure the output current. In addition, in the studies mentioned above, the contribution of the triboelectric effect also plays a role in improving the generated current. In our study, we try to eliminate the triboelectric contribution and generate a piezoelectric output power density of 0.029 ± 0.0013 $mWcm^{-2}$. Dia et al. [77]. fabricated a TENG based on electrospun PVDF/GO nanosheets, and cotton fibers were selected as a tribo-positive layer. PVDF/0.06 wt% GO- cotton fiber generated an output current of 35 μA for an area of 5 × 5 cm with a power density of 0.51 $mWcm^{-2}$. Shi et al. [64]. prepared PVDF-graphene (G) nanosheet-based TENG using PA6 as a positive tribo layer. The authors exhibited a higher energy harvesting performance of the TENG with power density of ~ 13.02 $mWcm^{-2}$ for PVDF/1.5 wt% G composite nanofiber. In this work, we have obtained the power density of 3.37 ± 0.72 $mWcm^{-2}$with an active area of 1.13 cm^2. However, in the literature, they have used a larger area of sample, and the high output power also comes from the differences in the measurement setup and the instruments. In the case of PyNG, no studies are reported based on rGO/PVDF electrospun composite. Nevertheless, the reported pyroelectric current output is low for the PVDF, and other fillers incorporated composite fiber. Sultana et al. [24]. demonstrated a methylammonium lead iodide incorporated electrospun PVDF PyNG. The authors performed a time-dependent temperature variation to assess the pyroelectric current by switching the IR light bulb on and off. A peak current of 17.75 pA was generated by PyNG. Similarly, Roy et al. [78]. showed the pyroelectric energy harvesting of PVDF/GO electrospun fiber using periodic illumination of IR light. Under temperature fluctuations, the device produced an output current of ~ 65 pA. You et al. [74]. prepared a PyNG consisting of TPU-carbon nanotube (CNTs) composite and electrospun poly (3,4-ethylenedioxythiophene): poly (styrene sulfonate)-polyvinyl pyrrolidone. Upon heating, the PyNG on the surface of a flexible polyimide heater could give a current value of 20 nA. Li et al. [73] conducted a similar experiment using a polyimide heater. The fabricated PVDF-ZnO generator produced an output current of 3 nA during the temperature

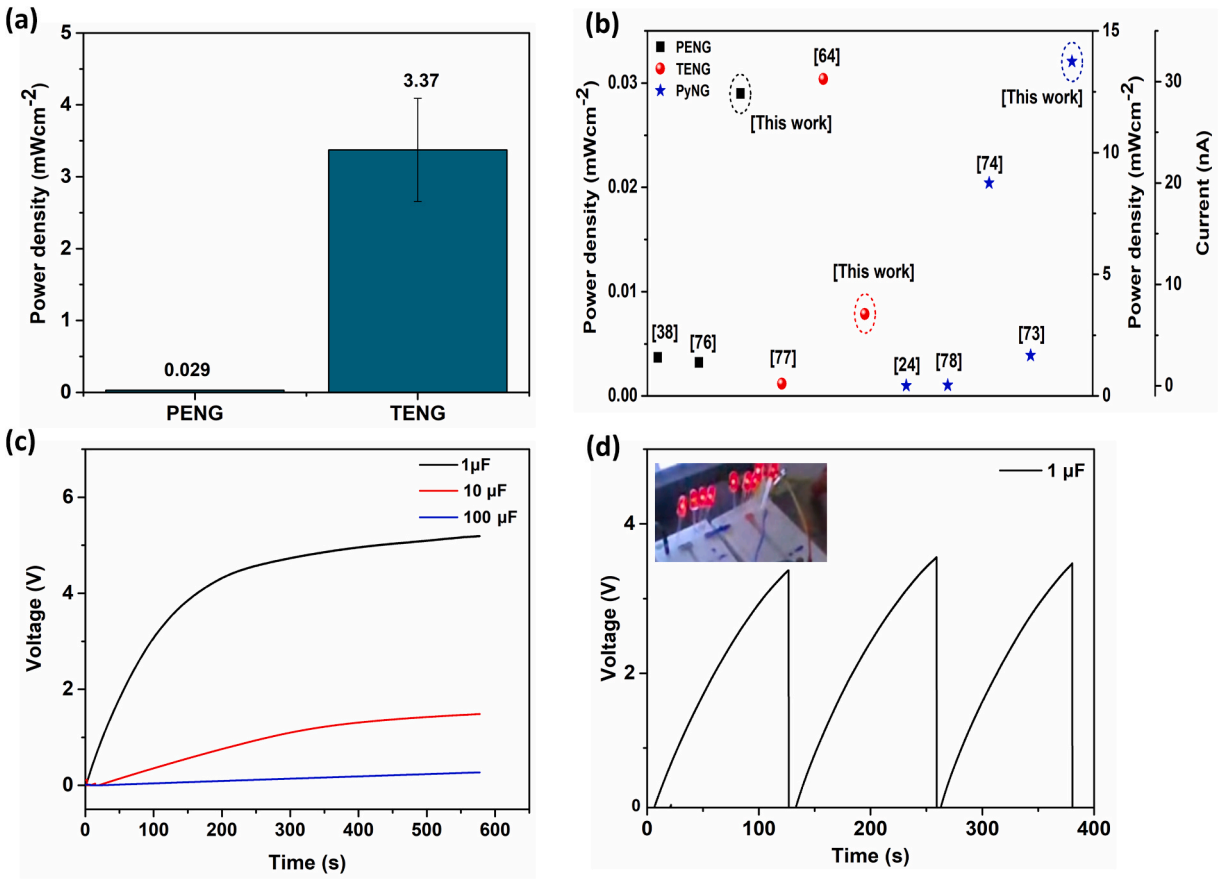

Fig. 6. (a) Power density of 7 wt%rGO/PVDF composite from the PENG and TENG (b) Reported energy harvesting performance of PENG, TENG, PyNG from the literature and this work (c) Charging curves of various capacitors (d) Cyclic charging and discharging behavior of 1 μF capacitor.

fluctuation. In the PyNG, as mentioned above, the authors claimed that the generated current signal is due to the pyroelectric effect. However, through this work, as discussed in detail in the pyroelectric characterization (section 3.3), we have observed a minimal current variation with temperature fluctuation, and that also might be a synergistic effect of the pyro and triboelectric effect. Also, the TSCs effect should be considered to avoid the false interpretation of the pyroelectric signal.

Furthermore, the charging of different capacitors using 7 wt% rGO/PVDF TENG is shown in Fig. 6c. The 1 μF capacitor can charge up to 5 V in 400 s and get saturated. In comparison, 10 and 100 μF capacitors reached 1.4 and 0.24 V, respectively. Fig. 6d represents the 1 μF capacitor charging and discharging characteristics of the TENG. Furthermore, to illustrate the practical feasibility of the 7 wt% rGO/PVDF composite fiber, the output power produced from the TENG is utilized to light 10 LEDs connected in series through a bridge rectifier. The corresponding video for the demonstration is provided in the supplementary information (Video S1). Thus, this study depicts a promising approach to enhance energy harvesting performance by incorporating a higher amount of rGO filler into the PVDF matrix. We have shown the multifunctionality, such as piezo-, tribo- and pyroelectric effects of the prepared composite and compared their properties at micro and macroscopic levels.

4. Conclusion

We have successfully incorporated a higher amount of rGO filler (1, 5, 7, 10 wt%) into the electrospun PVDF fiber and analyzed the effect of rGO for enhancing the electroactive β phase and crystallinity in PVDF/rGO composite fibers. Adding 7 wt% of rGO into the PVDF matrix increased the β phase to 81 % and crystallinity to 48.58 %, respectively. This is because rGO served as a nucleating agent and facilitated interfacial solid interaction between rGO and the PVDF chain. The rGO/PVDF composite can be used as a multifunctional nanogenerator to harvest the mechanical energy from the piezo and triboelectric effect and thermal energy from the pyroelectric effect. We presented a detailed study at the micro and macroscopic level to understand the behavior of single fiber and mat in terms of piezo, tribo, and pyroelectric effects. This would allow us to understand how the single fiber properties, such as piezoelectric amplitude, surface potential, thermal conductivity correlate with the bulk fiber mats piezo, tribo, and pyroelectric performance. From the piezoelectric characterizations, 7 wt% rGO/PVDF fibers showed 3 times higher piezo amplitude than pristine PVDF from PFM results. PENG with 7 wt% rGO generated an output power density of 1.29 ± 0.05 μWcm-2, 5 times higher than the pristine PVDF. Further, the surface potential results from KPFM showed that composite fiber has almost double the negative potential of the surface than the PVDF fiber. In alignment with the KPFM results, the 7 wt%rGO/PVDF TENG exhibited a higher triboelectric power output of 3.37 ± 0.72 $mWcm^{-2}$, whereas the PVDF based TENG generated a power output of 0.567 ± 0.08 $mWcm^{-2}$. For the thermal response, a very low current of 33 nA is generated from the 7 wt%rGO/PVDF PyNG, which is a synergetic effect from the pyro and triboelectric effects. For the first time, to the best of our knowledge, we distinguish piezo-, tribo-, and pyroelectric properties at both micro and macroscopic levels. Moreover, the energy generated by the TENG is stored in a 1μF capacitor and used to light up 10 LEDs. Hence, this study presents the importance of rGO addition into PVDF fiber and the improvement in the nanogenerator's interchangeable energy harvesting performance. Therefore, the rGO/PVDF multifunctional nanogenerator can be used in various environments to harvest ambient energy, serving as an excellent material for self-powered electronic

devices.

CRediT authorship contribution statement

Sunija Sukumaran: Writing – review & editing, Writing – original draft, Visualization, Validation, Methodology, Investigation, Formal analysis, Data curation, Conceptualization. **Piotr K. Szewczyk:** Writing – review & editing, Visualization, Methodology, Investigation, Formal analysis. **Tomasz Bajda:** Writing – review & editing, Resources, Methodology, Investigation. **Urszula Stachewicz:** Writing – review & editing, Writing – original draft, Supervision, Resources, Project administration, Methodology, Conceptualization.

Declaration of competing interest

The authors declare that they have no known competing financial interests or personal relationships that could have appeared to influence the work reported in this paper.

Acknowledgments

This study was conducted as part of the BioCom4SavEn project, which was funded by the European Research Council under the European Union's Horizon 2020 Framework Programme for Research and Innovation (ERC grant agreement no. 948840). The research project was also partly supported by the program "Excellence initiative—research university" for the AGH University of Krakow in Poland. We would like to acknowledge Adam Gaweł for helping with the XRD measurements.

Appendix A. Supplementary data

Supplementary data to this article can be found online at https://doi.org/10.1016/j.matdes.2025.114105.

Data availability

Data will be made available on request.

References

[1] Y. Qi, J. Zhao, J. Zeng, X. Cao, Y. Qin, J. Cao, L. Gong, X. Huang, Z. Wang, G. Liu, C. Zhang, Self-powered wireless temperature and vibration monitoring system by weak vibrational energy for industrial internet of things, ACS Appl. Mater. Interfaces 15 (2023) 40569–40578, https://doi.org/10.1021/acsami.3c08016.

[2] B.S. Athira, A. George, K. Vaishna Priya, U.S. Hareesh, E.B. Gowd, K.P. Surendran, A. Chandran, High-performance flexible piezoelectric nanogenerator based on electrospun PVDF-$BaTiO_3$ nanofibers for self-powered vibration sensing applications, ACS Appl. Mater. Interfaces 14 (2022) 44239–44250, https://doi.org/10.1021/acsami.2c07911.

[3] S.M.S. Rana, M.T. Rahman, M. Salauddin, S. Sharma, P. Maharjan, T. Bhatta, H. Cho, C. Park, J.Y. Park, Electrospun PVDF-TrFE/MXene Nanofiber Mat-Based Triboelectric Nanogenerator for Smart Home Appliances, ACS Appl. Mater. Interfaces 13 (2021) 4955–4967, https://doi.org/10.1021/acsami.0c17512.

[4] K.G. Motora, C.-M. Wu, G.M. Rani, W.-T. Yen, K.-S. Lin, Effect of electrode patterns on piezoelectric energy harvesting property of zinc oxide polyvinylidene fluoride based piezoelectric nanogenerator, Renew. Energy 217 (2023) 119208, https://doi.org/10.1016/j.renene.2023.119208.

[5] S. Divya, T.H. Oh, M. Bodaghi, 1D nanomaterial based piezoelectric nanogenerators for self-powered biocompatible energy harvesters, Eur. Polym. J. 197 (2023) 112363, https://doi.org/10.1016/j.eurpolymj.2023.112363.

[6] S. Sukumaran, S. Chatbouri, D. Rouxel, E. Tisserand, F. Thiebaud, T. Ben Zineb, Recent advances in flexible PVDF based piezoelectric polymer devices for energy harvesting applications, J. Intell. Mater. Syst. Struct. (2020) 1045389X20966058, https://doi.org/10.1177/1045389X20966058.

[7] A. Ali, H. Shaukat, S. Bibi, W.A. Altabey, M. Noori, S.A. Kouritem, Recent progress in energy harvesting systems for wearable technology, Energ. Strat. Rev. 49 (2023) 101124, https://doi.org/10.1016/j.esr.2023.101124.

[8] C. Zhi, S. Shi, Y. Si, B. Fei, H. Huang, J. Hu, Recent Progress of Wearable Piezoelectric Pressure Sensors Based on Nanofibers, Yarns, and Their Fabrics via Electrospinning, Adv. Mater. Technol. 8 (2023) 2201161, https://doi.org/10.1002/admt.202201161.

[9] V. Singh, B. Singh, MoS2-PVDF/PDMS based flexible hybrid piezo-triboelectric nanogenerator for harvesting mechanical energy, J. Alloy. Compd. 941 (2023) 168850, https://doi.org/10.1016/j.jallcom.2023.168850.

[10] Y. Wang, X. Cao, N. Wang, Recent Progress in Piezoelectric-Triboelectric Effects Coupled Nanogenerators, Nanomaterials 13 (2023) 385, https://doi.org/10.3390/nano13030385.

[11] K. Kim, S. Lee, J.-S. Nam, M. Joo, B. Mikladal, Q. Zhang, E.I. Kauppinen, I. Jeon, S. An, Highly Transparent and Mechanically Robust Energy-harvestable Piezocomposite with Embedded 1D P (VDF-TrFE) Nanofibers and Single-walled Carbon Nanotubes, Adv. Funct. Mater. 33 (2023) 2213374.

[12] S. Rana, V. Singh, B. Singh, Tailoring the Output Performance of PVDF-Based Piezo–Tribo Hybridized Nanogenerators via B, N-Codoped Reduced Graphene Oxide, ACS Appl. Electron. Mater. 4 (2022) 5893–5904, https://doi.org/10.1021/acsaelm.2c01085.

[13] A. Ben Ayed, A. Bouhamed, H. Nouri, N. Abdelmoula, H. Khemakhem, O. Kanoun, Robust and Flexible Piezoelectric Lead-Free Zn-BCZT/PVDF-HFP Nanogenerators for Wearable Energy Harvesting, ACS Appl. Electron. Mater. 5 (2023) 4282–4295, https://doi.org/10.1021/acsaelm.3c00562.

[14] W. Tang, T. Jiang, F.R. Fan, A.F. Yu, C. Zhang, X. Cao, Z.L. Wang, Liquid-Metal Electrode for High-Performance Triboelectric Nanogenerator at an Instantaneous Energy Conversion Efficiency of 70.6%, Adv. Funct. Mater. 25 (2015) 3718–3725, https://doi.org/10.1002/adfm.201501331.

[15] D. Choi, Y. Lee, Z.-H. Lin, S. Cho, M. Kim, C.K. Ao, S. Soh, C. Sohn, C.K. Jeong, J. Lee, others, Recent advances in triboelectric nanogenerators: from technological progress to commercial applications, ACS Nano 17 (2023) 11087–11219.

[16] A. Babu, K. Ruthvik, P. Supraja, M. Navaneeth, K.U. Kumar, R.R. Kumar, K. Prakash, N. Raju, High-performance triboelectric nanogenerator using ZIF-67/PVDF hybrid film for energy harvesting, J. Mater. Sci. Mater. Electron. 34 (2023) 2195.

[17] P.K. Szewczyk, A.E. Taşlı, J. Knapczyk-Korczak, U. Stachewicz, Steering triboelectric and mechanical properties of polymer fibers with carbon black, Compos. Sci. Technol. 243 (2023) 110247, https://doi.org/10.1016/j.compscitech.2023.110247.

[18] A. Babu, P. Malik, N. Das, D. Mandal, Surface potential tuned single active material comprised triboelectric nanogenerator for a high performance voice recognition sensor, Small 18 (2022) 2201331, https://doi.org/10.1002/smll.202201331.

[19] P. Costa, J. Nunes-Pereira, N. Pereira, N. Castro, S. Gonçalves, S. Lanceros-Mendez, Recent Progress on Piezoelectric, Pyroelectric, and Magnetoelectric Polymer-Based Energy-Harvesting Devices, Energ. Technol. 7 (2019) 1800852.

[20] Y. Yang, J.H. Jung, B.K. Yun, F. Zhang, K.C. Pradel, W. Guo, Z.L. Wang, Flexible pyroelectric nanogenerators using a composite structure of lead-free $KNbO_3$ nanowires, Adv. Mater. 24 (2012) 5357–5362, https://doi.org/10.1002/adma.201201414.

[21] C.R. Bowen, J. Taylor, E. LeBoulbar, D. Zabek, A. Chauhan, R. Vaish, Pyroelectric materials and devices for energy harvesting applications, Energy Environ. Sci. 7 (2014) 3836–3856, https://doi.org/10.1039/C4EE01759E.

[22] A. Thakre, A. Kumar, H.-C. Song, D.-Y. Jeong, J. Ryu, Pyroelectric energy conversion and its applications—flexible energy harvesters and sensors, Sensors 19 (2019) 2170, https://doi.org/10.3390/s19092170.

[23] G. Sebald, D. Guyomar, A. Agbossou, On thermoelectric and pyroelectric energy harvesting, Smart Mater. Struct. 18 (2009) 125006, https://doi.org/10.1088/0964-1726/18/12/125006.

[24] A. Sultana, S.K. Ghosh, M.M. Alam, P. Sadhukhan, K. Roy, M. Xie, C.R. Bowen, S. Sarkar, S. Das, T.R. Middya, D. Mandal, Methylammonium Lead Iodide Incorporated Poly(vinylidene fluoride) Nanofibers for Flexible Piezoelectric–Pyroelectric Nanogenerator, ACS Appl. Mater. Interfaces 11 (2019) 27279–27287, https://doi.org/10.1021/acsami.9b04812.

[25] Q. Wang, C.R. Bowen, W. Lei, H. Zhang, B. Xie, S. Qiu, M.-Y. Li, S. Jiang, Improved heat transfer for pyroelectric energy harvesting applications using a thermal conductive network of aluminum nitride in PMN–PMS–PZT ceramics, J. Mater. Chem. A 6 (2018) 5040–5051.

[26] P.D. Prasad, J. Hemalatha, Multifunctional films of poly(vinylidene fluoride)/ZnFe2O4 nanofibers for nanogenerator applications, J. Alloy. Compd. 854 (2021) 157189, https://doi.org/10.1016/j.jallcom.2020.157189.

[27] R.A. Surmenev, R.V. Chernozem, I.O. Pariy, M.A. Surmeneva, A review on piezo- and pyroelectric responses of flexible nano- and micropatterned polymer surfaces for biomedical sensing and energy harvesting applications, Nano Energy 79 (2021) 105442, https://doi.org/10.1016/j.nanoen.2020.105442.

[28] Q. Chen, Y. Cao, Y. Lu, W. Akram, S. Ren, L. Niu, Z. Sun, J. Fang, Hybrid piezoelectric/triboelectric wearable nanogenerator based on stretchable PVDF–PDMS composite films, ACS Appl. Mater. Interfaces 16 (2024) 6239–6249, https://doi.org/10.1021/acsami.3c15760.

[29] P.K. Szewczyk, A. Gradys, S.K. Kim, L. Persano, M. Marzec, A. Kryshtal, T. Busolo, A. Toncelli, D. Pisignano, A. Bernasik, S. Kar-Narayan, P. Sajkiewicz, U. Stachewicz, Enhanced Piezoelectricity of Electrospun Polyvinylidene Fluoride Fibers for Energy Harvesting, ACS Appl. Mater. Interfaces 12 (2020) 13575–13583, https://doi.org/10.1021/acsami.0c02578.

[30] P. Martins, A. Lopes, S. Lanceros-Mendez, Electroactive phases of poly (vinylidene fluoride): Determination, processing and applications, Prog. Polym. Sci. 39 (2014) 683–706.

[31] S. Sukumaran, P.K. Szewczyk, J. Knapczyk-Korczak, U. Stachewicz, Optimizing piezoelectric coefficient in PVDF fibers: key strategies for energy harvesting and smart textiles, Adv. Elect. Materials (2023) 2300404, https://doi.org/10.1002/aelm.202300404.

[32] S. Mishra, L. Unnikrishnan, S.K. Nayak, S. Mohanty, Advances in piezoelectric polymer composites for energy harvesting applications: a systematic review, Macromol. Mater. Eng. 304 (2019) 1800463, https://doi.org/10.1002/mame.201800463.

[33] S. An, H.S. Jo, G. Li, E. Samuel, S.S. Yoon, A.L. Yarin, Sustainable nanotextured wave energy harvester based on ferroelectric fatigue-free and flexoelectricity-enhanced piezoelectric P (VDF-TrFE) nanofibers with BaSrTiO3 nanoparticles, Adv. Funct. Mater. 30 (2020) 2001150.

[34] J. Xue, J. Xie, W. Liu, Y. Xia, Electrospun nanofibers: new concepts, materials, and applications, Acc. Chem. Res. 50 (2017) 1976–1987.

[35] C. Kumar, A. Gaur, S.K. Rai, P. Maiti, Piezo devices using poly(vinylidene fluoride)/reduced graphene oxide hybrid for energy harvesting, Nano-Struct. Nano-Objects 12 (2017) 174–181, https://doi.org/10.1016/j.nanoso.2017.10.006.

[36] H.M.A. Yaseen, S. Park, Enhanced power generation by piezoelectric P(VDF-TrFE)/rGO nanocomposite thin film, Nanomaterials 13 (2023) 860, https://doi.org/10.3390/nano13050860.

[37] M. Zeyrek Ongun, S. Oguzlar, E.C. Doluel, U. Kartal, M. Yurddaskal, Enhancement of piezoelectric energy-harvesting capacity of electrospun β-PVDF nanogenerators by adding GO and rGO, J Mater Sci: Mater Electron 31 (2020) 1960–1968, https://doi.org/10.1007/s10854-019-02715-w.

[38] J. Yang, Y. Zhang, Y. Li, Z. Wang, W. Wang, Q. An, W. Tong, Piezoelectric Nanogenerators based on Graphene Oxide/PVDF Electrospun Nanofiber with Enhanced Performances by In-Situ Reduction, Mater. Today Commun. 26 (2021) 101629, https://doi.org/10.1016/j.mtcomm.2020.101629.

[39] Y. Zeng, T. Li, Y. Yao, T. Li, L. Hu, A. Marconnet, Thermally conductive reduced graphene oxide thin films for extreme temperature sensors, Adv. Funct. Materials 29 (2019) 1901388, https://doi.org/10.1002/adfm.201901388.

[40] Y. Zi, L. Lin, J. Wang, S. Wang, J. Chen, X. Fan, P.-K. Yang, F. Yi, Z.L. Wang, Triboelectric–pyroelectric–piezoelectric hybrid cell for high-efficiency energy-harvesting and self-powered sensing, Adv. Mater. 27 (2015) 2340–2347, https://doi.org/10.1002/adma.201500121.

[41] S.K. Karan, R. Bera, S. Paria, A.K. Das, S. Maiti, A. Maitra, B.B. Khatua, An approach to design highly durable piezoelectric nanogenerator based on self-poled PVDF/AlO-rGO flexible nanocomposite with high power density and energy conversion efficiency, Adv. Energy Mater. 6 (2016) 1601016, https://doi.org/10.1002/aenm.201601016.

[42] C. Zhao, Q. Zhang, W. Zhang, X. Du, Y. Zhang, S. Gong, K. Ren, Q. Sun, Z.L. Wang, Hybrid piezo/triboelectric nanogenerator for highly efficient and stable rotation energy harvesting, Nano Energy 57 (2019) 440–449, https://doi.org/10.1016/j.nanoen.2018.12.062.

[43] S.K. Karan, S. Maiti, A.K. Agrawal, A.K. Das, A. Maitra, S. Paria, A. Bera, R. Bera, L. Halder, A.K. Mishra, J.K. Kim, B.B. Khatua, Designing high energy conversion efficient bio-inspired vitamin assisted single-structured based self-powered piezoelectric/wind/acoustic multi-energy harvester with remarkable power density, Nano Energy 59 (2019) 169–183, https://doi.org/10.1016/j.nanoen.2019.02.031.

[44] M.M. Abolhasani, K. Shirvanimoghaddam, M. Naebe, PVDF/graphene composite nanofibers with enhanced piezoelectric performance for development of robust nanogenerators, Compos. Sci. Technol. 138 (2017) 49–56, https://doi.org/10.1016/j.compscitech.2016.11.017.

[45] X. Cai, T. Lei, D. Sun, L. Lin, A critical analysis of the α, β and γ phases in poly (vinylidene fluoride) using FTIR, RSC Adv. 7 (2017) 15382–15389, https://doi.org/10.1039/C7RA01267E.

[46] S. Mireja, D.V. Khakhar, Methods to characterize the crystal polymorphs of polyvinylidene fluoride using Fourier transform infrared spectroscopy, Polym. Eng. Sci. 63 (2023) 2857–2870, https://doi.org/10.1002/pen.26410.

[47] A. Bužarovska, M. Kubin, P. Makreski, M. Zanoni, L. Gasperini, G. Selleri, D. Fabiani, C. Gualandi, PVDF/BaTiO3 composite foams with high content of β phase by thermally induced phase separation (TIPS), J. Polym. Res. 29 (2022) 272, https://doi.org/10.1007/s10965-022-03133-z.

[48] Ö.F. Ünsal, Y. Altın, A. Çelik Bedeloğlu, Poly(vinylidene fluoride) nanofiber-based piezoelectric nanogenerators using reduced graphene oxide/polyaniline, J. Appl. Polym. Sci. 137 (2020) 48517, https://doi.org/10.1002/app.48517.

[49] J.E. Lee, Y. Guo, R.E. Lee, S.N. Leung, Fabrication of electroactive poly(vinylidene fluoride) through non-isothermal crystallization and supercritical CO_2 processing, RSC Adv. 7 (2017) 48712–48722, https://doi.org/10.1039/C7RA09162A.

[50] P. Martins, C.M. Costa, S. Lanceros-Mendez, Nucleation of electroactive β-phase poly(vinilidene fluoride) with $CoFe_2O_4$ and NiFe2O4 nanofillers: a new method for the preparation of multiferroic nanocomposites, Appl. Phys. A 103 (2011) 233–237, https://doi.org/10.1007/s00339-010-6003-7.

[51] R. Imamura, A.B. Silva, R. Gregorio, γ→β Phase transformation induced in poly (vinylidene fluoride) by stretching, J. Appl. Polym. Sci. 110 (2008) 3242–3246, https://doi.org/10.1002/app.28851.

[52] P. Martins, A.C. Lopes, S. Lanceros-Mendez, Electroactive phases of poly (vinylidene fluoride): Determination, processing and applications, Prog. Polym. Sci. 39 (2014) 683–706, https://doi.org/10.1016/j.progpolymsci.2013.07.006.

[53] N.M.S. Hidayah, W.-W. Liu, C.-W. Lai, N.Z. Noriman, C.-S. Khe, U. Hashim, H.C. Lee, Comparison on graphite, graphene oxide and reduced graphene oxide: Synthesis and characterization, in: Penang, Malaysia, 2017: p. 150002. Doi: 10.1063/1.5005764.

[54] S. Janakiraman, A. Surendran, S. Ghosh, S. Anandhan, A. Venimadhav, Electroactive poly(vinylidene fluoride) fluoride separator for sodium ion battery with high coulombic efficiency, Solid State Ion. 292 (2016) 130–135, https://doi.org/10.1016/j.ssi.2016.05.020.

[55] N. Moazeni, M. Sadrjahani, A.A. Merati, M. Latifi, S. Rouhani, Effect of stimuli-responsive polydiacetylene on the crystallization and mechanical properties of PVDF nanofibers, Polym. Bull. 77 (2020) 5373–5388, https://doi.org/10.1007/s00289-019-03020-6.

[56] R. Gregorio, Determination of the α, β, and γ crystalline phases of poly(vinylidene fluoride) films prepared at different conditions, J Appl. Polymer Sci. 100 (2006) 3272–3279, https://doi.org/10.1002/app.23137.

[57] S.K. Karan, D. Mandal, B.B. Khatua, Self-powered flexible Fe-doped RGO/PVDF nanocomposite: an excellent material for a piezoelectric energy harvester, Nanoscale 7 (2015) 10655–10666.

[58] U. Stachewicz, P.K. Szewczyk, A. Kruk, A.H. Barber, A. Czyrska-Filemonowicz, Pore shape and size dependence on cell growth into electrospun fiber scaffolds for tissue engineering: 2D and 3D analyses using SEM and FIB-SEM tomography, Mater. Sci. Eng. C 95 (2019) 397–408, https://doi.org/10.1016/j.msec.2017.08.076.

[59] S. Shetty, S. Murugesan, S. Salehi, A. Pellert, M. Scheibel, T. Scheibel, S. Anandhan, Evaluation of piezoelectric behavior and biocompatibility of poly(vinylidene fluoride) ultrafine fibers with incorporated talc nanosheets, J Appl. Polymer Sci. 139 (2022) e52631, https://doi.org/10.1002/app.52631.

[60] X. Liu, S. Xu, X. Kuang, D. Tan, X. Wang, Nanoscale investigations on β-phase orientation, piezoelectric response, and polarization direction of electrospun PVDF nanofibers, RSC Adv. 6 (2016) 109061–109066, https://doi.org/10.1039/C6RA24473D.

[61] A. Baji, Y.-W. Mai, Q. Li, Y. Liu, Nanoscale investigation of ferroelectric properties in electrospun barium titanate/polyvinylidene fluoride composite fibers using piezoresponse force microscopy, Compos. Sci. Technol. 71 (2011) 1435–1440, https://doi.org/10.1016/j.compscitech.2011.05.017.

[62] Y. Jiang, L. Gong, X. Hu, Y. Zhao, H. Chen, L. Feng, D. Zhang, Aligned P(VDF-TrFE) nanofibers for enhanced piezoelectric directional strain sensing, Polymers 10 (2018) 364, https://doi.org/10.3390/polym10040364.

[63] A. Anand, D. Meena, K.K. Dey, M.C. Bhatnagar, Enhanced piezoelectricity properties of reduced graphene oxide (RGO) loaded polyvinylidene fluoride (PVDF) nanocomposite films for nanogenerator application, J. Polym. Res. 27 (2020) 358, https://doi.org/10.1007/s10965-020-02323-x.

[64] L. Shi, H. Jin, S. Dong, S. Huang, H. Kuang, H. Xu, J. Chen, W. Xuan, S. Zhang, S. Li, X. Wang, J. Luo, High-performance triboelectric nanogenerator based on electrospun PVDF-graphene nanosheet composite nanofibers for energy harvesting, Nano Energy 80 (2021) 105599, https://doi.org/10.1016/j.nanoen.2020.105599.

[65] R. Bhunia, S. Gupta, B. Fatma, R.K. Prateek, A.G. Gupta, Milli-Watt Power Harvesting from Dual Triboelectric and Piezoelectric Effects of Multifunctional Green and Robust Reduced Graphene Oxide/P(VDF-TrFE) Composite Flexible Films, ACS Appl, Mater. Interfaces 11 (2019) 38177–38189, https://doi.org/10.1021/acsami.9b13360.

[66] Z.L. Wang, Triboelectric Nanogenerators as New Energy Technology for Self-Powered Systems and as Active Mechanical and Chemical Sensors, ACS Nano 7 (2013) 9533–9557, https://doi.org/10.1021/nn404614z.

[67] Z.L. Wang, J. Chen, L. Lin, Progress in triboelectric nanogenerators as a new energy technology and self-powered sensors, Energy Environ. Sci. 8 (2015) 2250–2282.

[68] G. Zhu, J. Chen, T. Zhang, Q. Jing, Z.L. Wang, Radial-arrayed rotary electrification for high performance triboelectric generator, Nat. Commun. 5 (2014) 3426.

[69] T. Huang, M. Lu, H. Yu, Q. Zhang, H. Wang, M. Zhu, Enhanced power output of a triboelectric nanogenerator composed of electrospun nanofiber mats doped with graphene oxide, Sci. Rep. 5 (2015) 13942, https://doi.org/10.1038/srep13942.

[70] F. Calavalle, M. Zaccaria, G. Selleri, T. Cramer, D. Fabiani, B. Fraboni, Piezoelectric and electrostatic properties of electrospun PVDF-TrFE nanofibers and their role in electromechanical transduction in nanogenerators and strain sensors, Macromol. Mater. Eng. 305 (2020) 2000162.

[71] A. Moradi, P.K. Szewczyk, U. Stachewicz, Bridging a Gap in Thermal Conductivity and Heat Transfer in Hybrid Fibers and Yarns via Polyimide and Silicon Nitride Composites, Small (2023) 2305104, https://doi.org/10.1002/smll.202305104.

[72] C.-M. Wu, M.-H. Chou, T.F. Chala, Y. Shimamura, R. Murakami, Infrared-driven poly(vinylidene difluoride)/tungsten oxide pyroelectric generator for non-contact energy harvesting, Compos. Sci. Technol. 178 (2019) 26–32, https://doi.org/10.1016/j.compscitech.2019.05.004.

[73] G.-Y. Li, H.-D. Zhang, K. Guo, X.-S. Ma, Y.-Z. Long, Fabrication and piezoelectric-pyroelectric properties of electrospun PVDF/ZnO composite fibers, Mater. Res. Express 7 (2020) 095502, https://doi.org/10.1088/2053-1591/abb264.

[74] M.-H. You, X.-X. Wang, X. Yan, J. Zhang, W.-Z. Song, M. Yu, Z.-Y. Fan, S. Ramakrishna, Y.-Z. Long, A self-powered flexible hybrid piezoelectric–pyroelectric nanogenerator based on non-woven nanofiber membranes, J. Mater. Chem. A 6 (2018) 3500–3509.

[75] S. Jachalke, E. Mehner, H. Stöcker, J. Hanzig, M. Sonntag, T. Weigel, T. Leisegang, D.C. Meyer, How to measure the pyroelectric coefficient? Appl. Phys. Rev. 4 (2017) 021303 https://doi.org/10.1063/1.4983118.

[76] M. Sekkarapatti Ramasamy, A. Rahaman, B. Kim, Effect of phenyl-isocyanate functionalized graphene oxide on the crystalline phases, mechanical and piezoelectric properties of electrospun PVDF nanofibers, Ceram. Int. 47 (2021) 11010–11021, https://doi.org/10.1016/j.ceramint.2020.12.223.

[77] Y. Dai, X. Zhong, T. Xu, Y. Li, Y. Xiong, S. Zhang, High-Performance triboelectric nanogenerator based on electrospun polyvinylidene fluoride-graphene oxide nanosheet composite nanofibers, Energ. Technol. 11 (2023) 2300426, https://doi.org/10.1002/ente.202300426.

[78] K. Roy, S.K. Ghosh, A. Sultana, S. Garain, M. Xie, C.R. Bowen, K. Henkel, D. Schmeiβer, D. Mandal, A self-powered wearable pressure sensor and pyroelectric breathing sensor based on GO interfaced PVDF nanofibers, ACS Appl. Nano Mater. 2 (2019) 2013–2025, https://doi.org/10.1021/acsanm.9b00033.